JEM Journal of Experimental Medicine

ARTICLE

p38α–eIF6–Nsun2 axis promotes ILC3's rapid response to protect host from intestinal inflammation

Jida Huang[1,2,3,4*], Jing Zhang[1,2,3,4*], Panwei Song[1,2,3,4], Jiaoyan Huang[1,2,3], Zi Yang[5], Jiahuai Han[6], Li Wu[1,2,3], and Xiaohuan Guo[1,2,3,4,7]

Group 3 innate lymphoid cells (ILC3s) are important for maintaining gut homeostasis. Upon stimulation, ILC3s can rapidly produce cytokines to protect against infections and colitis. However, the regulation of ILC3 quick response is still unclear. Here, we find that eIF6 aggregates with Nsun2 and cytokine mRNA in ILC3s at steady state, which inhibits the methyltransferase activity of Nsun2 and the nuclear export of cytokine mRNA, resulting in the nuclear reservation of cytokine mRNA. Upon stimulation, phosphorylated p38α phosphorylates eIF6, which in turn releases Nsun2 activity, and promotes the nuclear export of cytokine mRNA and rapid cytokine production. Genetic disruption of p38α, Nsun2, or eIF6 in ILC3s influences the mRNA nuclear export and protein expression of the protective cytokines, thus leading to increased susceptibility to colitis. Together, our data identify a crucial role of the p38α–eIF6–Nsun2 axis in regulating rapid ILC3 immune response at the posttranscriptional level, which is critical for gut homeostasis maintenance and protection against gut inflammation.

Introduction

Inflammatory bowel disease (IBD), also known as ulcerative colitis and Crohn's disease, has steadily increased its burden on public health in both developed and developing countries (Kaplan, 2015). Although multiple pathological mechanisms have been identified in IBD, the pathogenesis of the disease is still poorly understood. Interactions between host and environmental factors are important in the development and progression of IBD (Lavelle and Sokol, 2020). Among the host factors, the intestinal mucosal immune system plays a major role in maintaining intestinal homeostasis. In addition to harboring many harmless symbiotic bacteria and food antigens, the intestinal tract is also often challenged by pathogenic microorganisms. It is therefore necessary for the intestinal mucosal immune system to respond efficiently and differently to different environmental stimuli to prevent excessive inflammation and fight infection. Dysregulation of intestinal mucosal immunity always leads to infectious or inflammatory diseases, including IBD. Within gut tissue, a significant component of mucosal immunity is the group 3 innate lymphoid cell (ILC3), a group of recently defined lymphocytes lacking expression of rearranged antigen-specific cell receptors. ILC3s predominantly accumulate in the gut, where they serve as sentinels to maintain gut homeostasis (Goldberg et al., 2015). A study has shown that IBD patients have a reduced number of ILC3s and dysregulated ILC3 functions (Goc et al., 2021). ILC3s are capable of rapidly responding to environmental signaling, such as cytokines, metabolic signals, and microbiota (Goldberg et al., 2015), and producing a series of effector molecules, such as IL-22, GM-CSF, and IL-17A. Through these effector molecules, ILC3s interact with many other cells within the mucosal environment and play crucial roles in various infectious and inflammatory diseases (Castellanos et al., 2018; Guo et al., 2014; Hu et al., 2023; Huang et al., 2022; Wang et al., 2020, 2023). However, the specific mechanism by which ILC3s acquire the ability to respond rapidly to environmental cues remains unknown.

The MAPK signaling pathway plays an essential role in enabling cells to sense extracellular signals and orchestrate appropriate responses. MAPK activation has been observed in the

[1]Institute for Immunology, Tsinghua University, Beijing, China; [2]School of Basic Medical Sciences, Tsinghua University, Beijing, China; [3]Beijing Key Lab for Immunological Research on Chronic Diseases, Tsinghua University, Beijing, China; [4]State Key Laboratory of Molecular Oncology, School of Basic Medical Sciences, Tsinghua University, Beijing, China; [5]Protein Preparation and Identification Facilities at Technology Center for Protein Science, School of Life Sciences, Tsinghua University, Beijing, China; [6]State Key Laboratory of Cellular Stress Biology, School of Life Sciences, Innovation Center for Cell Signaling Network, Xiamen University, Xiamen, China; [7]SXMU-Tsinghua Collaborative Innovation Center for Frontier Medicine, Shanxi Medical University, Taiyuan, China.

*J. Huang and J. Zhang contributed equally to this paper. Correspondence to Xiaohuan Guo: guoxiaohuan@tsinghua.edu.cn.

gut tissues of both UC and CD patients (Waetzig et al., 2002). Notably, the p38MAPK–NF-κB pathway is pivotal for regulating the expression of inflammatory mediators such as *Tnfa*, *Cox2*, and *Il1b* (Coskun et al., 2011), suggesting that inhibiting MAPKs, particularly p38MAPK, may have therapeutic benefits. However, both clinical trials and animal experiments have demonstrated a dichotomous role for p38MAPK inhibition in colitis (Coskun et al., 2011; ten Hove et al., 2002), indicating that p38MAPK may play distinct roles in different cells within the gut environment. The specific features of p38MAPK in different intestinal cells need to be further investigated.

In this study, we observed that p38MAPK signaling is significantly activated in intestinal ILC3s in a model of dextran sodium sulfate (DSS)-induced colitis. Further research suggests that p38α plays a critical role in the rapid cytokine production by intestinal ILC3s. Specific p38α deletion in ILC3s causes increased intestinal inflammation. Mechanistically, upon stimulation, phosphorylated p38α quickly enters the nucleus, regulates the eIF6/Nsun2/mRNA paraspeckle complex, and promotes the rapid nuclear export and translation of cytokine transcripts in ILC3s, suggesting that the p38–eIF6–Nsun2 pathway may be a potential target for modulating ILC3 function and treating intestinal inflammatory diseases.

Results

p38α in hematopoietic cells protects mice from DSS-induced colitis

To assess the role of MAPKs in colitis, we examined the activation levels of different MAPK members in the colon tissue of mice treated with DSS. 3 days after exposure to 3% DSS, increased p38α phosphorylation was primarily observed in CD45$^+$ immune cells (Fig. S1 A), in contrast to predominant ERK and JNK signaling in EpCAM$^+$ colonic epithelial cells (Fig. S1, B and C), suggesting a potential role of p38α in immune cells during the development of DSS-induced colitis. Thus, hemopoietic p38α deletion *Vav*^{icre}*Mapk14*$^{fl/fl}$ mice were generated to determine the role of p38α in colitis. In comparison with their littermate control *Mapk14*$^{fl/fl}$ mice, *Vav*^{icre}*Mapk14*$^{fl/fl}$ mice experienced more severe body weight loss and higher mortality rates after receiving DSS treatment (Fig. 1, A and B). To explore which immune cell was regulated by p38α in colitis, p38α phosphorylation in different immune cell types after DSS exposure was examined. Interestingly, ILC3s exhibited significant p38α phosphorylation upon DSS exposure, as evidenced by flow cytometry and immunofluorescence staining (Fig. 1, C and D), indicating that p38α is activated in ILC3s during early colitis. Consistently, multiple proinflammatory cytokines including IL-1β and IL-23 were able to significantly activate p38α phosphorylation in ILC3s in vitro (Fig. 1 E). To examine the effect of p38α activation in ILC3s, colonic ILC3s from naïve mice or mice with DSS-induced colitis were isolated and their cytokine production was assessed. The deficiency of p38α significantly restricted the production of IL-22 and GM-CSF by ILC3s from mice treated with or without DSS (Fig. 1, F and G). Together, these data indicate that the p38α signaling is activated in ILC3s during colitis development, and p38α in hematopoietic cells is required for the protection against DSS-induced colitis.

p38α in ILC3s is crucial for maintaining intestinal homeostasis and preventing intestinal inflammation

To further verify the intrinsic role of p38α in ILC3s, *Rorc*^{cre}*Mapk14*$^{fl/fl}$ mice were generated to specifically delete p38α in RORγt$^+$ cells, including ILC3s and T cells. In the naïve state, the deficiency of *Mapk14* didn't affect the development of ILC3 subsets, proliferation, and cell viability (Fig. S2, A–C). In line with the phenotypes observed in *Vav*^{icre}*Mapk14*$^{fl/fl}$ mice (Fig. 1, A and B), *Rorc*^{cre}*Mapk14*$^{fl/fl}$ mice developed more severe colitis than *Mapk14*$^{fl/fl}$ mice after DSS challenge, as evidenced by more body weight loss, shorter colons, and more severe colon pathology (Fig. 2, A–C). p38α-deficient ILC3s also exhibited a significant reduction of IL-22 and GM-CSF production by flow cytometry (Fig. 2 D). To exclude the effect of p38α defect in T cells in *Rorc*^{cre}*Mapk14*$^{fl/fl}$ mice, *Cd4*^{cre}*Mapk14*$^{fl/fl}$ mice were generated and challenged with DSS-induced colitis. Compared with control mice, *Cd4*^{cre}*Mapk14*$^{fl/fl}$ mice displayed slightly less body weight loss and longer colons (Fig. 2, E and F), suggesting that p38α in T cells is not required for the protection against DSS-induced colitis. Moreover, IL-22 supplementation significantly ameliorated colitis in *Rorc*^{cre}*Mapk14*$^{fl/fl}$ mice (Fig. 2, G and H) Interestingly, at around 20 wk of age, *Rorc*^{cre}*Mapk14*$^{fl/fl}$ mice developed spontaneous colon inflammation, characterized by abnormal colon structure and histological score (Fig. 2 I). Collectively, these data demonstrate that p38α in ILC3s is essential for maintaining intestinal homeostasis and preventing colon inflammation.

p38α promotes rapid cytokine production in ILC3s through a posttranscriptional mechanism

To determine how p38α controls ILC3 response, we first examined the level of mRNA expression of various cytokines in the colonic tissues of DSS-treated *Rorc*^{cre}*Mapk14*$^{fl/fl}$ mice and control *Mapk14*$^{fl/fl}$ mice. In accordance with previous findings (Fig. 2, A–C), *Rorc*^{cre}*Mapk14*$^{fl/fl}$ mice showed higher levels of proinflammatory cytokines, such as *Il1b*, *Il6*, and *Ccl2* than control mice (Fig. S2 D). However, IL22 and GM-CSF mRNA expression levels were comparable between *Mapk14*$^{fl/fl}$ and *Rorc*^{cre}*Mapk14*$^{fl/fl}$ mice (Fig. S2 D), which is inconsistent with their protein expression levels in ILC3s, implying that p38α regulates ILC3 cytokine production through a posttranscriptional mechanism. To elucidate the underlying mechanisms, ILC3s were isolated and stimulated with IL-1β at different time points (0, 5, 15, 60, 120 min) in vitro, and the kinetics of p38α activation and IL-22 production were assessed by western blot and ELISA, respectively. IL-1β treatment robustly increased p38α phosphorylation within 5 min (Fig. 3, A and B) and significantly promoted IL-22 production within 30 min (Fig. 3 B), suggesting that p38α activation may facilitate the rapid response of ILC3s. Additionally, compared with the control cells, p38α-deficient ILC3s did not show any reduction of the expression of the IL-1β receptor or significant induction of the expression of negative p38α regulator DUSP1/4/8 (Fig. S2, E and F), suggesting that the impaired response in p38α-deficient ILC3s might not be the result of the defective IL-1 receptor machinery or an elevated negative regulation of cytokine translation. Interestingly, compared with the control group, ILC3s treated with α-amanitin, a specific inhibitor

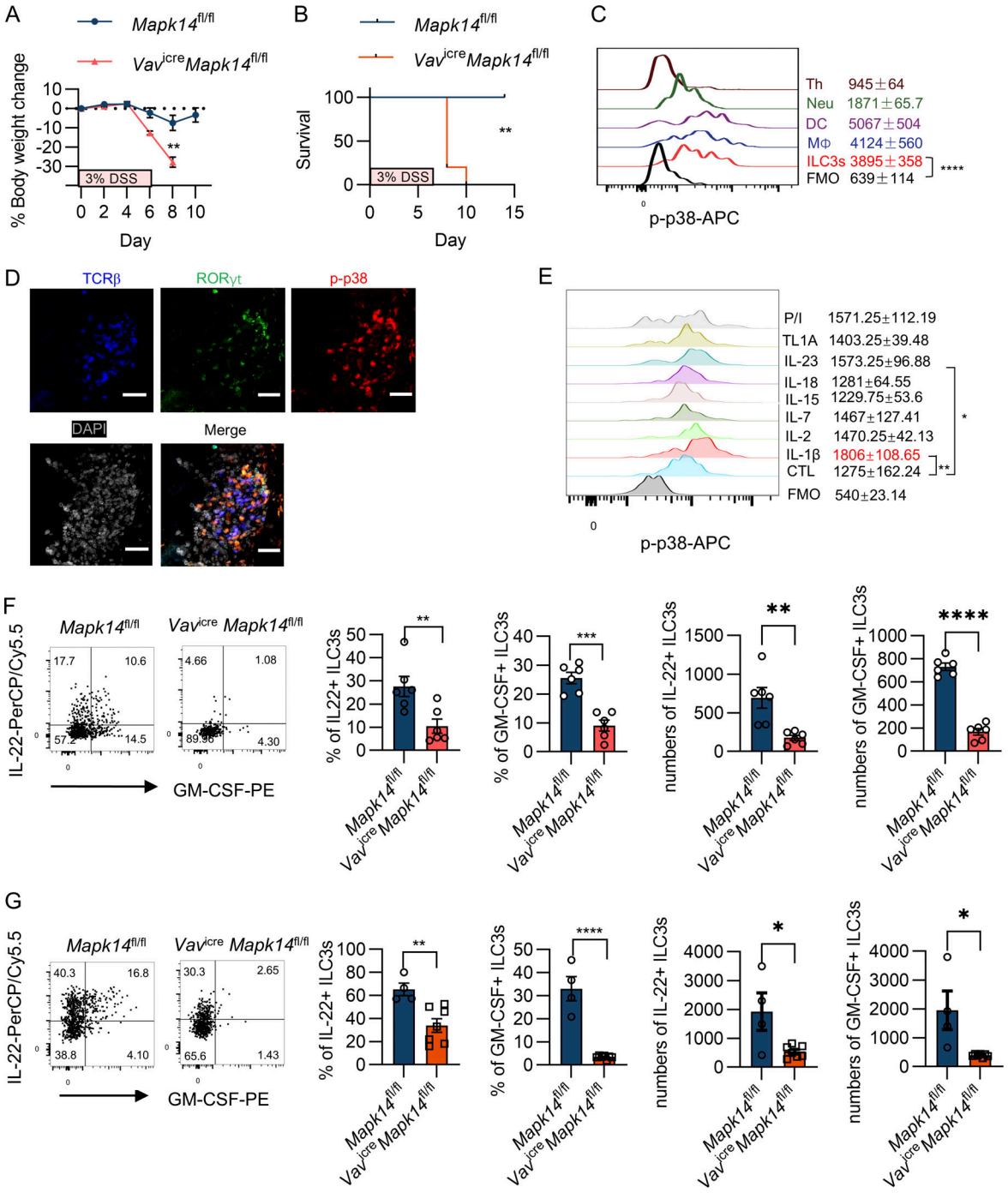

Figure 1. **p38α in hematopoietic cells protects mice from DSS-induced colitis. (A–C)** 8-wk-old mice were given 3% DSS in drinking water for 6 days, followed by normal drinking water. The body weight change (A) and survival (B) of *Vav*^{icre} *Mapk14*$^{fl/fl}$ (n = 5) and their littermates *Mapk14*$^{fl/fl}$ mice (n = 6) were measured. **(C)** At day 3 after DSS treatment, the colonic LPLs from wild type mice (n = 4) were isolated and analyzed by flow cytometry. Representative flow cytometry and mean fluorescence intensity (MFI) of p-p38 in Th (gating in CD45$^+$CD90$^+$CD3$^+$CD4$^+$), neutrophil (gating in CD45$^+$Gr-1$^+$CD11b$^+$), DC (gating in CD45$^+$MHCII$^+$CD11c$^+$), macrophage (MΦ, gating in CD45$^+$F4/80$^+$CD11b$^+$), and ILC3s (gating in CD45^{low}CD90^{high}) were shown. FMO represents fluorescence minus one control. **(D)** *Rorc*$^{gfp/+}$ reporter mice were exposed to 3% DSS for 3 days. Phosphorylated p38α in RORγt$^+$TCRβ$^-$ ILC3s from colon was shown. Scale bars, 20 µm. **(E)** The isolated LPLs from the small intestine and colon were stimulated with different stimuli for 60 min in vitro and p-p38 in ILC3s (gating in CD45^{low}CD90^{high}) was measured by flow cytometry. MFIs of p-p38 were shown. FMO represents fluorescence minus one control. **(F)** Representative flow cytometry and pooled analysis of IL-22 and GM-CSF production by ILC3s (gating in CD45$^+$CD90$^+$TCRβ$^-$RORγt$^+$). The colonic LPLs from naive *Vav*^{icre}*Mapk14*$^{fl/fl}$ (n = 6) or *Mapk14*$^{fl/fl}$ (n = 6) littermate mice were in vitro–stimulated by PMA/ionomycin. **(G)** 8-wk-old *Vav*^{icre}*Mapk14*$^{fl/fl}$ (n = 7) and their littermates *Mapk14*$^{fl/fl}$ (n = 4) were given 3% DSS in drinking water. At day 3, after DSS treatment, the colonic LPLs were ex vivo–stimulated by PMA/ionomycin and representative flow cytometry, and pooled analysis of IL-22 and GM-CSF production by ILC3s (gating in CD45$^+$CD90$^+$TCRβ$^-$RORγt$^+$) were shown. Data are representative of one of two independent experiments (A–E). Each symbol represents an individual mouse from two pooled experiments (F and G). Data are mean ± SEM and two-tailed Student's unpaired t test (A, F, and G), log-rank (Mantel–Cox) test (B) were used for statistical analysis. *P < 0.05, **P < 0.01, ****P < 0.0001, ns, no significant difference.

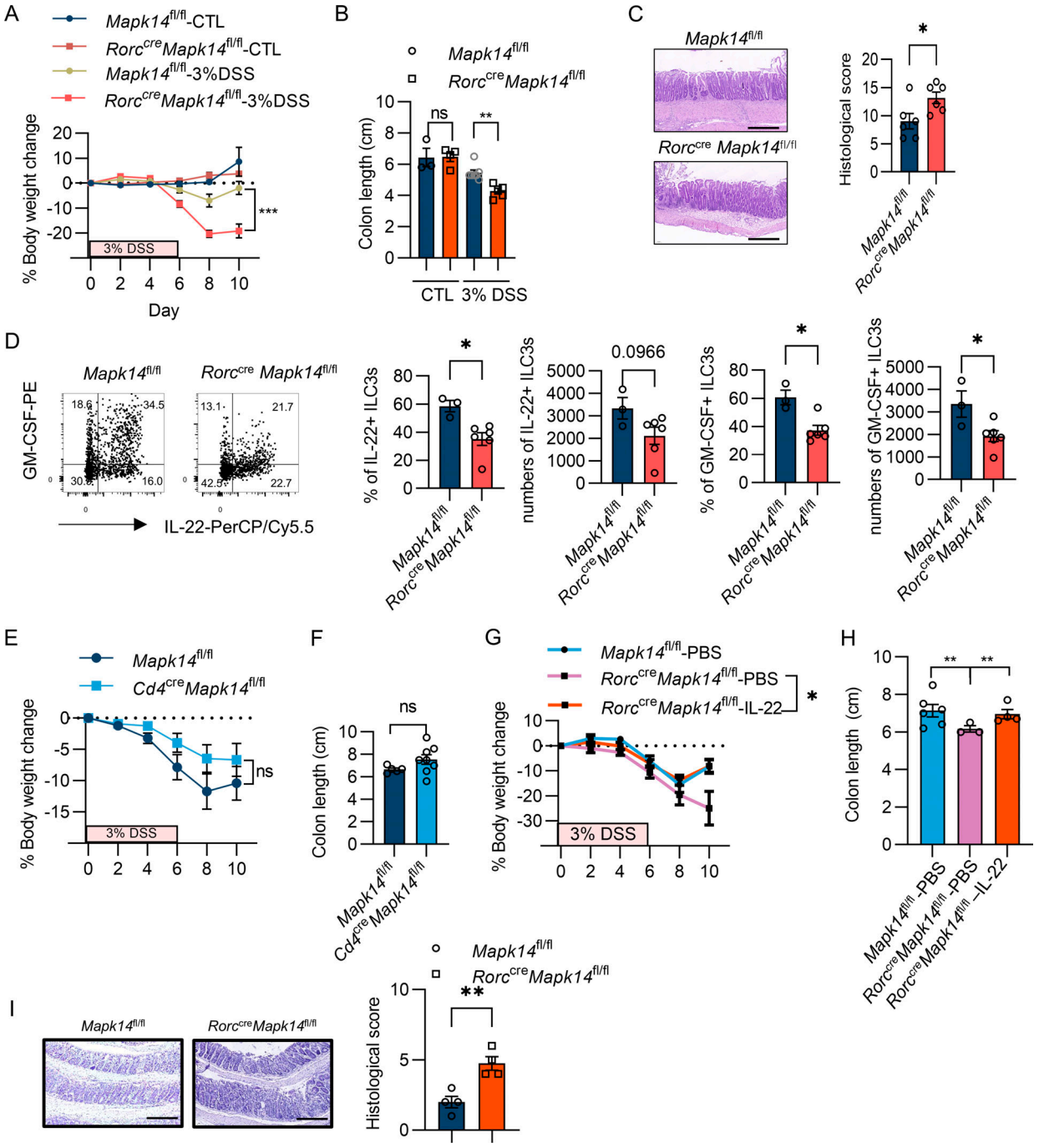

Figure 2. **p38α in ILC3s is crucial for maintaining intestinal homeostasis and preventing intestinal inflammation. (A–C)** 8-wk-old mice were exposed to 3% DSS for 6 days. **(A)** Body weight change curves of DSS-treated (*Rorc*^{cre}*Mapk14*$^{fl/fl}$, *n* = 13; *Mapk14*$^{fl/fl}$, *n* = 13) or control mice (*Rorc*^{cre}*Mapk14*$^{fl/fl}$, *n* = 9; *Mapk14*$^{fl/fl}$, *n* = 10) were shown. **(B)** The colon length of DSS-treated (*Rorc*^{cre}*Mapk14*$^{fl/fl}$, *n* = 7; *Mapk14*$^{fl/fl}$, *n* = 5) or control mice (*Rorc*^{cre}*Mapk14*$^{fl/fl}$, *n* = 4; *Mapk14*$^{fl/fl}$, *n* = 3) were measured. **(C)** The colons of *Rorc*^{cre}*Mapk14*$^{fl/fl}$ (*n* = 6) and *Mapk14*$^{fl/fl}$ mice (*n* = 6) were collected for H&E staining at day 10 after DSS treatment. Gross morphological changes of colons and colitis score were shown. Scale bars, 250 µm. **(D)** Representative flow cytometry and pooled analysis of IL-22 and GM-CSF production by ILC3s (gating in CD45$^+$CD90$^+$TCRβ$^-$RORγt$^+$) from colonic LPLs of *Rorc*^{cre}*Mapk14*$^{fl/fl}$ (*n* = 4) or *Mapk14*$^{fl/fl}$ (*n* = 4) littermate mice after 3 days of DSS exposure. **(E and F)** *Cd4*^{cre}*Mapk14*$^{fl/fl}$ (*n* = 7) and *Mapk14*$^{fl/fl}$ (*n* = 7) mice were given 3% DSS in drinking water for 6 days. Body weight change curves (E) and colon length (F) were shown. **(G and H)** 8-wk-old *Mapk14*$^{fl/fl}$ or *Rorc*^{cre}*Mapk14*$^{fl/fl}$ mice were administrated with PBS or IL-22 and treated with 3% DSS for 6 days (PBS-*Rorc*^{cre}*Mapk14*$^{fl/fl}$, *n* = 3; PBS-*Rorc*^{cre}*Mapk14*$^{fl/fl}$, *n* = 4, *Mapk14*$^{fl/fl}$, *n* = 6). Body weight changes (G) and the colon lengths (H) were shown. **(I)** Representative colonic histology and colitis score of naïve *Rorc*^{cre}*Mapk14*$^{fl/fl}$ (*n* = 4) and littermate mice (*n* = 4) around 20-wk old. Scale bars, 250 µm. Data are representative of one of two independent experiments (D, G, and H). Two experiments were pooled together (A, C, E, and I). Each dot (B–I) represents one individual mouse. Data are mean ± SEM, and two-tailed Student's unpaired *t* test (A–I) were used for statistical analysis. *P < 0.05, **P < 0.01, ***P < 0.001; ns, no significant difference.

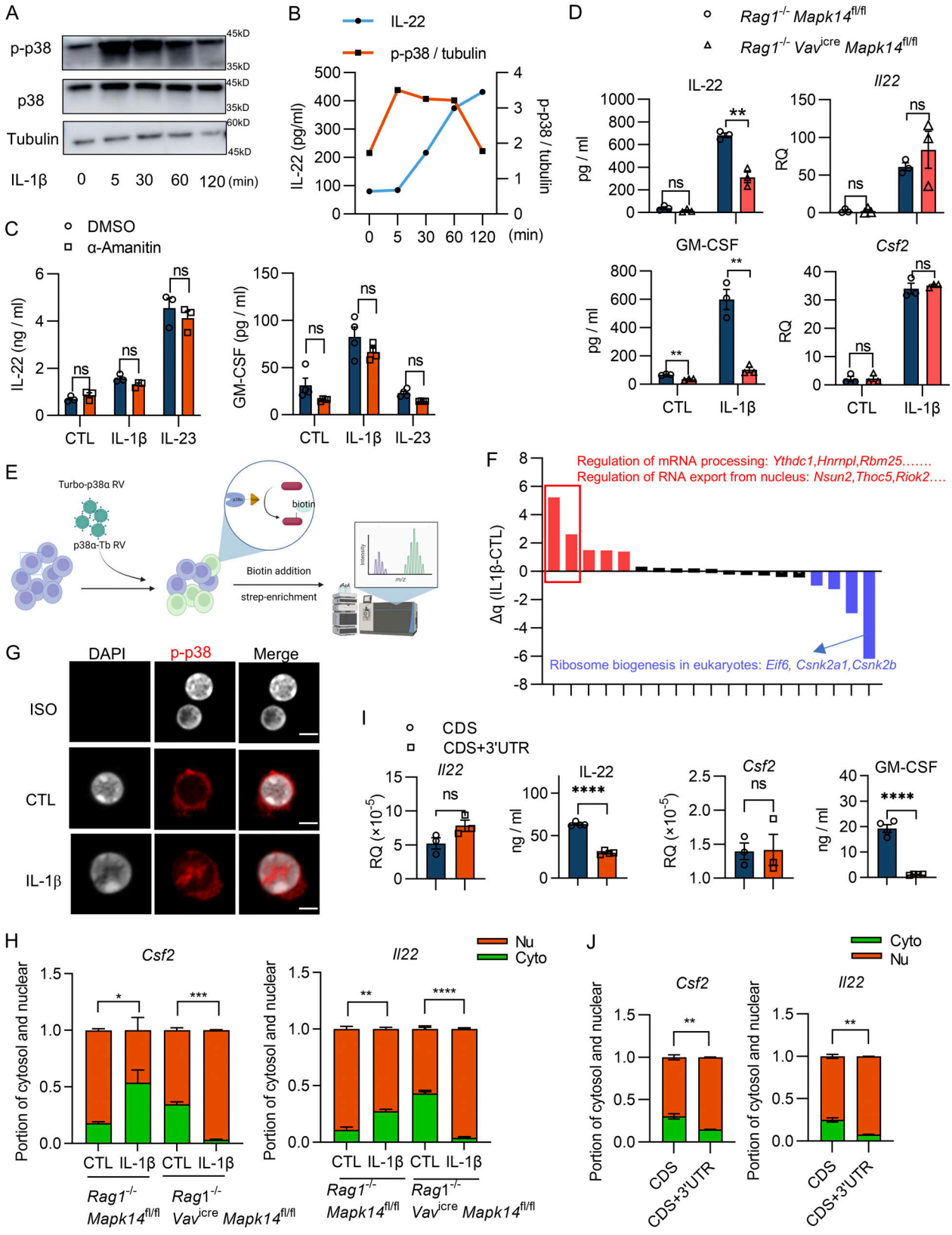

Figure 3. **p38α promotes rapid cytokine production through regulating mRNA nuclear export in ILC3s. (A and B)** ILC3s sorted from murine small intestine and colon (gated in 7-ADD$^-$CD45^{low}CD90$^+$) were treated with IL-1β at different time points. **(A)** Protein levels of total and phosphorylated p38α were shown. Tubulin was detected as a loading control. **(B)** IL-22 in the culture supernatant was examined by ELISA. The concentration of IL-22 and activation of p38α comparison in time course. **(C)** LPLs from the small intestine and colon lamina propria were pre-treated with or without α-Amanitin and then stimulated with IL-1β and IL-23 in vitro. The production of IL-22 and GM-CSF were detected by ELISA after 18 h stimulation. **(D)** ILC3s were sorted from the small intestine

and colon LPLs of *Rag1*$^{-/-}$*Mapk14*$^{fl/fl}$ and *Rag1*$^{-/-}$*Vav*^{icre}*Mapk14*$^{fl/fl}$ mice and then were stimulated with IL-1β and IL-23 for 18 h. The protein (left) and mRNA expression levels (right) of IL-22 and GM-CSF were examined by ELISA and qPCR. **(E)** The diagram of TurboID-based proximity labeling for capturing the p38α-interactome. **(F)** The GO differential analysis of p38α-interactome between control and IL-1β treatment group. **(G)** Representative immunofluorescence images of p-p38 in ILC3s. The sorted ILC3s (gated in 7-ADD^{-}CD45^{low}CD90^{high}) were stimulated with or without IL-1β for 5 min in vitro. Scale bars, 4 µm. **(H)** ILC3s (gated in 7-ADD^{-}CD45^{low}CD90^{high}) sorted from the small intestine and colon of *Rag1*$^{-/-}$*Mapk14*$^{fl/fl}$ and *Rag1*$^{-/-}$*Vav*^{icre}*Mapk14*$^{fl/fl}$ mice were stimulated with or without IL-1β. The nuclear and cytosol mRNA were fractionated and the distribution of transcripts were analyzed by qPCR. The cytosol fractions in each group were compared for statistical analysis. **(I and J)** The vectors containing *Il22/Csf2* CDS or CDS+3′UTR were delivered into 293T cells. **(I)** The mRNA and protein expression levels of IL-22 and GM-CSF were examined by qPCR (left) and ELISA (right). **(J)** The nuclear and cytosol mRNA were fractionated and analyzed by qPCR. Data are representative of one of two independent experiments (A–D and G–J). Each dot (C, D, and I) represents one biological replicate. Data are mean ± SEM and statistical significance was tested by two-tailed Student's unpaired *t* test (C, D, and H–J), *P < 0.05, **P < 0.01, ***P < 0.001, ****P < 0.0001; ns, no significant difference. Source data are available for this figure: SourceData F3.

of RNA polymerase II blocking RNA synthesis, showed no reduction in IL-22 and GM-CSF production following IL-1β or IL-23 stimulation (Fig. 3 C and Fig. S2 G), suggesting that the rapid cytokine response by ILC3s is independent of new transcript synthesis. Moreover, compared with cells from *Mapk14*$^{fl/fl}$ mice, intestinal lamina propria leukocytes (LPLs) from *Rorc*^{cre}*Mapk14*$^{fl/fl}$ mice exhibited lower protein secretion levels, but higher mRNA expression levels, of IL-22 and GM-CSF after IL-1β or IL-23 treatment in vitro (Fig. S2, H–J). Consistently, sorted p38α-sufficient and p38α-deficient ILC3s displayed significantly different levels of IL-22 and GM-CSF protein expression, but similar mRNA expression levels after IL-1β stimulation in vitro (Fig. 3 D). Additionally, the IL-17A and IFNγ production was also significantly reduced by p38α-deficient ILC3s (Fig. S2 K), suggesting p38α regulates a variety of cytokine expression in ILC3s. Since IL-23 is also considered a major stimulatory molecule for ILC3s, the kinetics of IL-22 production at both protein and mRNA levels were examined in isolated ILC3s stimulated with IL-23 at different time points in vitro. Although the *Il22* mRNA level was higher in p38α-deficient ILC3s than control ILC3s at a late time point, the IL-22 protein production was significantly reduced in p38α-deficient ILC3s after IL-23 stimulation (Fig. S2 L), indicating that p38α is also required for the optimal IL-23-mediated cytokine production in ILC3s. However, compared with untreated ILC3s, IL-23 was still able to promote IL-22 production in *Mapk14*-deficient ILC3s, suggesting an alternative IL-23-mediated pathway for cytokine generation in ILC3s. Interestingly, *Mapk14* deficiency also led to decreased production of IL-5 in ILC2s and IFNγ in ILC1s at both protein and mRNA levels (Fig. S2 M), indicating that p38α plays a role in all ILCs but may do so through different mechanisms. Together, these data support that p38α may enable ILC3s to initiate a rapid immune response to environmental cues through a posttranscriptional mechanism.

p38α nuclear localization promotes nuclear export of the cytokine mRNA in ILC3s after IL-1β stimulation

MAPKAP-K2 (MK2) is the most well-known p38α substrate and can directly inactivate eEF2K and promote translation (Ronkina et al., 2019; Stoecklin et al., 2004). Thus, to further determine whether the p38α–MK2 axis governs the posttranscriptional regulation of ILC3 cytokine production, intestinal LPLs were treated with two different p38α inhibitors: SB203580, which inhibits p38 MAPK catalytic activity by binding to the ATP-binding pocket and CMPD1, which is a selective and non-ATP-competitive p38MAPK-mediated MK2 phosphorylation inhibitor. Interestingly, only SB203580, but not CMPD1, significantly suppressed the expression of IL-22 and GM-CSF by ILC3s (Fig. S3 A), indicating that p38α regulating the ILC3 rapid response might be independent of MK2. Enzyme-catalyzed proximity labeling (PL), such as TurboID labeling (Branon et al., 2018), is an effective approach to studying rapidly dynamic interactions, such as enzyme–substrate interactions. To investigate the downstream mechanism of p38α in ILC3s, TurboID-based PL of p38α was performed in MNK-3 cells, an ILC3 cell line (Allan et al., 2015), with or without IL-1β stimulation (Fig. 3 E and Table S1). According to gene ontology (GO) differential analysis of mass spectrometry (MS) data, the p38α-interactome revealed an enrichment in the RNA export pathway and regulation of the mRNA processing pathway upon IL-1β stimulation, while p38α showed more interactions with proteins involved in ribosome biogenesis pathway without IL-1β treatment (Fig. 3 F and Table S2). Many components of the RNA export pathway and RNA processing pathway reside in the nucleus, and immunofluorescence analysis also suggested that phosphorylated p38α was primarily located in the nucleus after IL-1β stimulation (Fig. 3 G), indicating that p38α might translocate into nuclear and promote cytokine mRNA export or processing upon stimulation.

Since we found that the majority transcripts of *Il22* and *Csf2* might be mature mRNA through reverse transcription PCR (RT-PCR) with specific primer pairs that spanned the intron (Fig. S3 B), the subcellular proportion of mRNA localization was further examined. The mRNA subcellular fractionation analysis showed that a majority of *Il22* and *Csf2* mRNA was located in the nucleus of naive ILC3s and then were exported into cytosol upon IL-1β stimulation in control ILC3s (Fig. 3 H). However, in p38α-deficient ILC3s, most of the mRNA for *Il22* and *Csf2* was trapped in the nucleus following IL-1β stimulation (Fig. 3 H), suggesting that the IL-1β–p38α axis controls nuclear export of the cytokine mRNA to cytosol in ILC3s. Collectively, these data indicate that p38α may drive rapid ILC3 responses by facilitating nuclear export of the cytokine mRNAs upon environmental challenge.

Various mechanisms mediate mRNA retention in the nucleus, such as retained introns (Wegener and Muller-McNicoll, 2018). Beyond the intron cis-elements, cis-elements within the 3′ untranslated region (3′UTR) are also involved in regulating mRNA localization (Andreassi and Riccio, 2009). Since the majority of the transcripts of *Il22* and *Csf2* are mature mRNA in ILC3s, we examined whether the 3′UTR of *Il22* and *Csf2* mRNA is critical for their localization. The vectors containing IL-22 and GM-CSF coding sequence (CDS) with or without their respective

3′UTRs were overexpressed in 293T cells. Results showed that the presence of 3′UTRs significantly reduced the protein production of IL-22 and GM-CSF without affecting the abundance of their mRNAs (Fig. 3 I). Additionally, mRNA subcellular fractionation revealed that the 3′UTRs present in the cytokine-expressing vectors enhanced RNA retention within the nucleus (Fig. 3 J). Together, these data indicate that the 3′UTR of *Il22* and *Csf2* mRNA may control cytokine production by regulating mRNA nuclear export in ILC3s.

The IL-1β–p38α axis promotes nuclear export of mRNA and the protein production of ILC3 cytokines by disrupting the eIF6/mRNA paraspeckle

Next, to investigate possible trans-elements that regulate the 3′UTRs of cytokine mRNAs for nucleus retention in ILC3s, biotinylated IL-22 CDS mRNAs with or without 3′UTRs were incubated with cell lysates from ILC3s treated with or without IL-1β, and then mRNA binding proteins were isolated and analyzed by MS (Fig. 4, A and B). Eight proteins exhibited potential interactions with the 3′UTR of IL-22 mRNAs in naive ILC3s but not in ILC3s following IL-1β stimulation (Fig. 4, B and C; and Table S3), indicating they may be candidates for regulating IL-22 mRNA nuclear retention in ILC3s. To determine the mechanism of p38α-dependent regulation of mRNA nuclear retention, the 3′UTR-interactome and TurboID-p38α-interactome (Table S1) were analyzed interactively (Fig. 4 C), revealing eIF6 as a promising candidate (Fig. 4 C). Co-immunoprecipitation (co-IP) experiments with MNK-3 cells demonstrated that eIF6 could interact with phosphorylated p38α (Fig. 4 D). Biacore surface plasmon resonance (SPR) assay showed that purified p38α could bind to purified eIF6 with an affinity around 1.159 μM (Fig. 4 E), further supporting their direct interaction. Moreover, combined single-molecule fluorescent in situ hybridization (smFISH) and immunofluorescent staining assays revealed that most IL-22 mRNA was located in the nucleus and colocalized with eIF6 in naive MNK-3 cells (Fig. 4 F), indicating that eIF6 may interact with IL-22 mRNA. Interestingly, we observed that eIF6 was distributed in spots within the nucleus of ILC3s (Fig. 4, F and G). As trapping in the nuclear speckle or paraspeckle is one of the mechanisms responsible for mRNA nuclear retention, we hypothesized that eIF6 could regulate IL-22 mRNA nuclear retention through the formation of a puncta or speckle structure. In line with our speculation, IL-1β stimulation significantly reduced the fluorescence intensity of eIF6 puncta (Fig. 4 G), possibly due to the translocation of eIF6 from the nucleus to the cytoplasm (Fig. 4 H). More importantly, p38α inhibitor SB203580 treatment completely blocked the effect of IL-1β on eIF6 translocation and nuclear puncta dissipation (Fig. 4, G and H), indicating that p38α activation may directly impact eIF6 puncta in the ILC3 nucleus. Additionally, the purified eIF6 protein also displayed an increase in size relative to the prediction according to size exclusion chromatography (Fig. S3 C), which implies that eIF6 is self-aggregating. Together, these findings suggest that eIF6 may be an important component of the IL-1β–p38α axis regulating cytokine mRNA nuclear export in ILC3s.

Further, overexpression of eIF6 in MNK-3 cells significantly decreased the production of IL-22 and GM-CSF proteins as compared with the control group (Fig. 4 I), and knockdown of eIF6 with shRNA significantly improved IL-22 and GM-CSF production in MNK-3 cells (Fig. 4 J) as well as in p38α-deficient ILC3s (Fig. 4 K). Additionally, mRNA subcellular fractionation analysis revealed that overexpression of eIF6 in MNK-3 cells significantly enhanced RNA retention within the nucleus compared with the control group (Fig. 4 L). Collectively, our data suggest that eIF6 may aggregate with cytokine mRNAs and retain them in the nucleus of naïve ILC3s, and activated p38α signaling could promote cytokine mRNA nuclear export through regulating eIF6.

eIF6 prevents nuclear export of cytokine mRNAs through inhibiting the methyltransferase activity of Nsun2 in ILC3s

According to our previous analysis (Fig. 3 E and Table S1), the p38α-interactome showed enrichment in the RNA export pathway, including Nsun2. Nsun2 is an important RNA methyltransferase that catalyzes the 5-methylcytosine (m^5C) modification in mRNAs. This modification could be recognized by the mRNA export adaptor and is essential for mRNA nuclear export (Yang et al., 2017). Thus, we hypothesized that Nsun2 might be the target of IL-1β–p38α–eIF6 axis for cytokine mRNA export in ILC3s. Co-IP assays confirmed that Nsun2 could interact with both phosphorylated-p38α and eIF6 (Fig. 5 A). Interestingly, after IL-1β treatment, the interaction between Nsun2 and p-p38α was enhanced, while the interaction between Nsun2 and eIF6 was reduced in MNK-3 cells (Fig. 5 B), indicating that the interaction between p38α and eIF6 may influence the interaction between Nsun2 and eIF6. Furthermore, with combined smFISH and immunofluorescent staining assays, we observed that Nsun2 was colocalized with IL-22 mRNA and eIF6 puncta in naïve MNK-3 cells (Fig. 5 C). IL-1β stimulation led to a dissipation of eIF6 puncta and also a dissociation of IL-22 mRNA from Nsun2 and eIF6, with increased IL-22 mRNA in the cytosol, which were all inhibited by the addition of p38α inhibitor SB203580 (Fig. 5 C). Together, these findings suggest that the IL-1β–p38α axis promotes IL-22 mRNA nuclear export through eIF6 regulating Nsun2.

Next, to determine how eIF6 regulates Nsun2, an RNA methylation assay with purified eIF6 and Nsun2 was conducted in vitro, followed by high-performance liquid chromatography-MS (HPLC-MS) for methylated cytosine detection. Results showed that eIF6 significantly decreased the ratio of methylated cytosine to unmethylated cytosine (Fig. 5 D), suggesting that eIF6 could directly inhibit the methyltransferase activity of Nsun2 in vitro. Moreover, an RNA dot blot with anti-m^5C antibody showed that IL-1β stimulation could significantly induce mRNA m^5C modification in MNK-3 cells (Fig. 5 E and Fig. S3 D). And knockdown of eIF6 with shRNA dramatically increased the level of mRNA m^5C modification (Fig. 5 E). Taken together, these data suggest that eIF6 may prevent nuclear export of cytokine mRNAs through inhibiting Nsun2 catalyzing mRNA m^5C modification in ILC3s, while the IL-1β–p38α axis could relieve this inhibition by regulating eIF6.

eIF6 may inhibit Nsun2 methyltransferase activity through blocking the access of S-adenosyl methionine (SAM) to the catalytic center

To further determine the specific mechanism of eIF6 inhibiting Nsun2 enzyme activity, AlphaFold2 was used to predict the

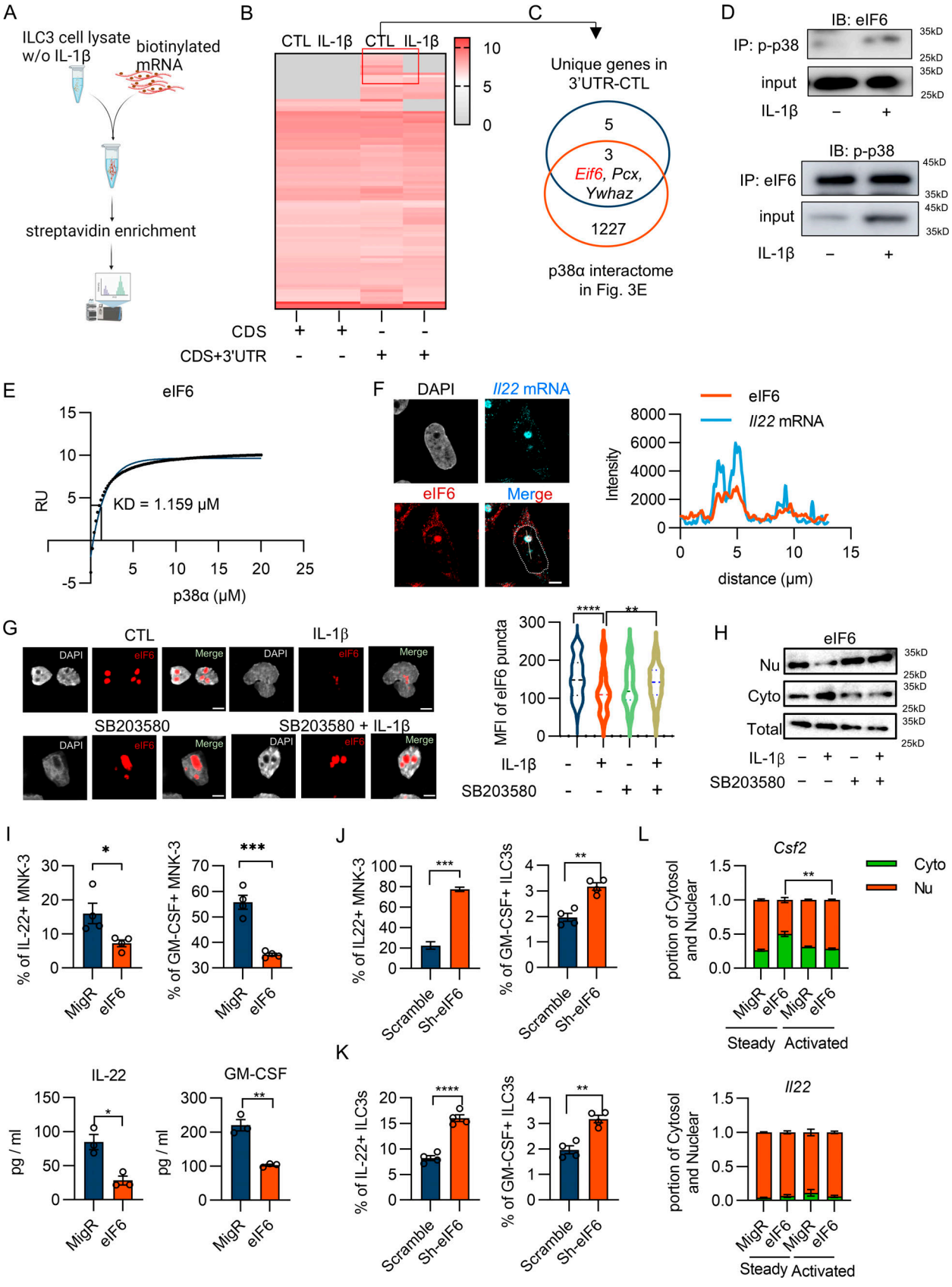

Figure 4. **The IL-1β–p38α axis promotes mRNA nuclear export and protein production of ILC3 cytokines by disrupting the eIF6/mRNA paraspeckle.** **(A–C)** The biotinylated *Il22* CDS mRNAs with or without 3′UTRs were incubated with cell lysates from ILC3s treated with or without IL-1β, and then mRNA binding proteins were isolated and analyzed by MS. **(A)** The diagram of strategy for screening of IL-22 mRNA 3′UTR-interactome. **(B)** The mRNA-interactome

identified by MS. **(C)** The Venn diagram shows the interactive analysis with the unique 3′UTR-interactome and TurboID-p38α-interactome. **(D)** Western blot analysis of the co-IP between p-p38α and eIF6 in MNK-3 cells treated with or without IL-1β. **(E)** The binding affinity between p38α and eIF6 was measured by Biacore SPR assay. eIF6 was attached to the CM-5 chips and the indicated flow phases were delivered to the Biscore system. **(F)** Representative images of immunofluorescent staining of eIF6 (red) and smFISH of *Il22* mRNA (cyan) in MNK-3 cells. Line traces (white arrow in merged inset) of fluorescence intensity from images. Scale bars, 5 µm. **(G)** Representative immunofluorescence images of eIF6 (red) in MNK-3 cells after 2 h of IL-1β treatment with or without p38α inhibitor SB203580. The MFI of eIF6 puncta was analyzed by ImageJ. Scale bars, 5 µm. **(H)** Quantification of eIF6 protein in nuclear and cytosol of MNK-3 cells with or without IL-1β and SB203580 treatment. **(I)** eIF6-overexpressing MNK-3 cells were constructed via infection with eIF6-expressing retrovirus. IL-22 and GM-CSF production were examined by flow cytometry (top) and ELISA (bottom). **(J)** eIF6-knock-down MNK-3 cells were constructed via infection with retrovirus containing shRNA against eIF6. IL-22 and GM-CSF production were examined by flow cytometry. **(K)** eIF6 was knocked-down through retrovirus containing shRNA against eIF6 in p38α-deficient ILC3s. The protein expression of IL-22 and GM-CSF were examined by flow cytometry. **(L)** Control and eIF6-overexpressing MNK-3 cells were stimulated with IL-1β, IL-23 and PMA/ionomycin. The nuclear and cytosol mRNA were fractionated and analyzed by qPCR. Data are representative of one of two independent experiments (D–L). Each dot (I and K) represents one biological replicate. Dissociation-one phase decay is applied to fit KD (E). Data are mean ± SEM and statistical significance was tested by two-tailed Student's unpaired *t* test (G and I–L), *P < 0.05, **P < 0.01, ***P < 0.001, ****P < 0.0001. Source data are available for this figure: SourceData F4.

potential eIF6-Nsun2 interaction pattern. The structural information indicates that eIF6 and Nsun2 probably interact at Glu8/Asn9 sites of eIF6 and Lys219/Asp217 sites of Nsun2 (Fig. 5 F). Interestingly, the eIF6-Nsun2 interaction surface is located on the SAM binding pocket of Nsun2 (Fig. 5 F), potentially preventing SAM from accessing the catalytic center of Nsun2. Next, the interaction pattern of Nsun2, eIF6, and SAM was analyzed through Biacore SPR assay. Nsun2 and eIF6 exhibit an equilibrium dissociation constant (KD) of 1.47 µM (Fig. 5 G), while Nsun2 and SAM exhibit a KD of 0.203 µM (Fig. 5 H). The addition of 15 µM eIF6 dramatically altered the Nsun2–SAM interaction curve (Fig. 5 I), indicating that eIF6 could disrupt SAM–Nsun2 interaction. Consistently, the SAM (1 µM) addition also disrupted Nsun2–eIF6 interaction (Fig. 5 J), suggesting that eIF6 and SAM may competitively bind to Nsun2 and consequently impact the methyltransferase activity of Nsun2. Furthermore, mutation of eIF6 interacting residues (Glu8/Asn9 to Ala8/Gly9, referred to as $eIF6^{EN\text{-}AG}$) significantly decreased KD to 44.5 µM (Fig. 5 K). Mutant $eIF6^{EN\text{-}AG}$ also showed an abolished inhibitory effect on cytokine production in MNK-3 cells compared with wild type $eIF6^{WT}$ (Fig. 5 L), suggesting that the eIF6 may interact with Nsun2 and regulate ILC3 cytokine expression through Glu8/Asn9 residues.

Nsun2 in ILC3s is required for the cytokine production and protection against colitis

Next, to further examine the role of Nsun2 in ILC3s, $Rorc^{cre}Nsun2^{fl/fl}$ mice were generated to delete Nsun2 in RORγt$^+$ ILC3s. Although Nsun2 deficiency did not influence the percentages and numbers of ILC3s in the colon of naive mice (Fig. 6 A), Nsun2-deficient ILC3s produced less IL-22, GM-CSF, and IL-17A after IL-1β, IL-23, or PMA/ionomycin stimulation (Fig. 6 B; and Fig. S4, A and B), indicating the important role of Nsun2 in controlling ILC3 responses. Consistent with p38α-deficient ILC3s, Nsun2-deficient ILC3s also did not show any reduction of the expression of IL-1β receptor or induction of the expression of negative p38α regulator DUSP1/4/8 (Fig. S4 C). Moreover, after a challenge with 3% DSS, $Rorc^{cre}Nsun2^{fl/fl}$ mice exhibited more significant body weight loss (Fig. 6 C), accompanied by fewer ILC3s expressing IL-22 and GM-CSF than their $Nsun2^{fl/fl}$ counterparts (Fig. 6 D). To exclude Nsun2 effect in T cells in $Rorc^{cre}Nsun2^{fl/fl}$ mice, we also treated $Cd4^{cre}Nsun2^{fl/fl}$ mice with 3% DSS, and the results showed that Nsun2 deficiency in T cells could attenuate DSS-induced colitis (Fig. 6 E), which is consistent with previous report (Yang et al., 2023). Together, these data suggest that Nsun2 regulates IL-22 and GM-CSF production in ILC3s and is required to protect the host against colitis.

G3BP1 assists p38α in phosphorylating eIF6 and promotes ILC3 immune response

We next sought to explore how p38α regulates eIF6. A previous study has shown that eIF6 can be phosphorylated by GSK3β at the C-terminal, which is important for eIF6 translocation (Jungers et al., 2020). Interestingly, the structural analysis by AlphaFold2 also suggests that the C-terminal helix of eIF6 hangs off the main structure, making it accessible for post-translational modification (Fig. 5 F). Since p38α is a MAPK kinase that phosphorylates many different substrates, we hypothesized that it may directly phosphorylate eIF6's C-terminal. According to the protein phosphorylation prediction software GPS (Xue et al., 2008), multiple sites of p38MAPK phosphorylation at the C-terminal of eIF6 have been predicted, even with higher scores than GSK3β (Fig. S5 A). Additionally, mutation of Ser243 ($eIF6^{S243A}$) or all seven serine and threonine residues at the C-terminal of eIF6 ($eIF6^{7ST\text{-}A}$) significantly suppressed cytokine production in MNK-3 cells (Fig. 7 A), supporting the notion that eIF6 C-terminal phosphorylation is required for ILC3 immunity. However, the direct phosphorylation of eIF6 by p38α was scarcely detected in vitro (data not shown). A previous study suggests that substrates with docking sequences could bind to the docking site of p38α and stabilize the catalytic conformation, thus enhancing the affinity and phosphorylation activity (Tokunaga et al., 2014). Although eIF6 has a docking sequence, it is buried within its main structure. Thus, we speculate that other proteins may provide docking sequences to facilitate p38α catalyzing eIF6 phosphorylation. To identify the potential factors, the eIF6-interactome was examined by immunoprecipitation with anti-eIF6 antibody followed by MS in ILC3s (Table S4). Following the analysis of the eIF6-interactome with the p38α-TURBO-interactome, 35 potential candidates were identified to be interacting with both eIF6 and p38α (Fig. 7 B and Table S5). GO enrichment analysis revealed that these proteins were highly enriched in the mRNA processing pathway and negative regulation of mRNA metabolism (Fig. 7 C). One of the 35 candidates, G3BP1, has multiple p38α docking sequences (Fig.7 D). To determine whether G3BP1 is involved in p38α

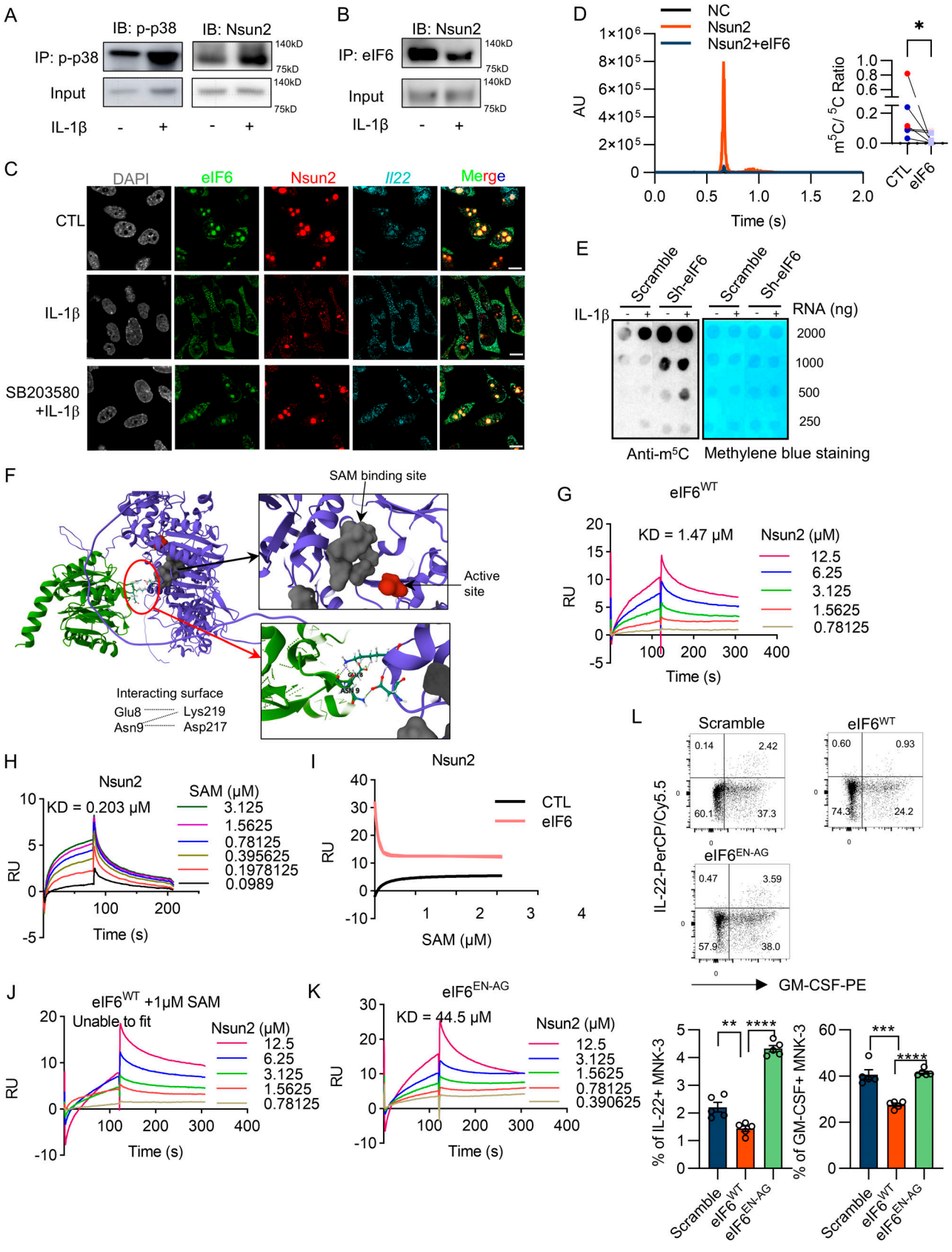

Figure 5. **eIF6 prevents the nuclear export of cytokine mRNAs by inhibiting the methyltransferase activity of Nsun2 in ILC3s. (A and B)** Western blot analysis of the co-IP between p-p38α and Nsun2 (A) or between eIF6 and Nsun2 (B) in MNK-3 cells treated with or without IL-1β. **(C)** Representative images of immunofluorescent staining of eIF6 (green), Nsun2 (red), and smFISH of *Il22* mRNA (cyan) in MNK-3 cells stimulated with or without IL-1β and SB203580. Scale

bars, 10 µm. **(D)** The Nsun2-mediated m^5C assay with purified eIF6 and Nsun2 protein was conducted in vitro. The *Il22* (red dot) or *Csf2* (blue dot) mRNA was synthesized in vitro. Nsun2-mediated m^5C modification on the cytokine transcripts with Nsun2 (red) or with Nsun2 plus eIF6 (blue) was performed. Then the mRNA was purified and digested to single nucleotide. The m^5C modification was determined by HPLC-MS (left). The ratios of methylated cytosine to unmethylated cytosine were shown (right). Data are pooled from two independent experiments. **(E)** RNA dot blot analysis of mRNAs with m^5C modification in control or eIF6-knocked-down MNK-3 cells with or without IL-1β stimulation. **(F)** The potential eIF6 (green)-Nsun2 (purple) interaction pattern predicted by AlphaFold2. The SAM binding pocket (gray) of Nsun2 and the interactive surface (ball and stick presented) are shown. The dash lines between amino acids indicate the hydrogenic bone of Nsun2/eIF6 complex. **(G)** The binding affinity between wild type eIF6 ($eIF6^{WT}$) and Nsun2 was measured by Biacore SPR assay. $eIF6^{WT}$ was attached to the CM-5 chips and the indicated Nsun2 flow phase was delivered to the Biacore system. **(H)** The binding affinity between Nsun2 and SAM was measured by Biacore SPR assay. Nsun2 was attached to the CM-5 chips and the indicated SAM flow phase was delivered to the Biacore system. **(I)** The binding affinity between Nsun2 (fixed phase) and SAM in the presence of eIF6 was measured by Biacore SPR assay. **(J)** The binding affinity between $eIF6^{WT}$ (fixed phase) and Nsun2 in the presence of SAM was measured by Biacore SPR assay. **(K)** The binding affinity between mutant $eIF6^{EN\text{-}AG}$ (fixed phase) and Nsun2 was measured by Biacore SPR assay. **(L)** The control and WT or mutant eIF6-overexpression MNK-3 cells were activated and the cytokine production was analyzed by flow cytometry. Data are representative of one of two independent experiments (A–E and G–L). Each dot (D and L) represents one biological replicate. Biacore Insight Evaluation software (GE Healthcare) is applied to calculate the KD (G–K). Data are mean ± SEM and statistical significance was tested by two-tailed Student's unpaired *t* test (L), two-tailed Student's paired *t* test (D), *P < 0.05, **P < 0.01, ***P < 0.001, ****P < 0.0001. Source data are available for this figure: SourceData F5.

phosphorylating eIF6, we first examined the interaction between G3BP1 and both eIF6 and p38α. Co-IP assays showed that G3BP1 interacted with both phosphorylated p38α and eIF6 in MNK-3 cells after IL-1β stimulation (Fig. 7 E), and Biacore SPR assay revealed that the binding affinity of eIF6 to G3BP1 was ∼9.72 µM (Fig.7 F). Moreover, an in vitro kinase assay coupled with Phos-tag SDS-PAGE analysis revealed that G3BP1 significantly facilitated the phosphorylation of eIF6 by p38α (Fig.7 G). Based on the in vitro kinase assay and Phos-tag/MS, there are multiple p38α phosphorylation sites on the C-terminal of eIF6 (Fig. S5 B). Collectively, these data demonstrate that G3BP1 functions as a cofactor for p38α-mediated phosphorylation of eIF6. Furthermore, epigallocatechin gallate (EGCG), an inhibitor of G3BP1 (Liu et al., 2019), significantly reduced IL-22 and GM-CSF protein production in ILC3s (Fig. 7, H and I) without altering their mRNA expression (Fig. 7 J), indicating that G3BP1 also modulates ILC3 cytokine production posttranscriptionally.

Discussion

The mucosal and skin barrier tissues are primary interfaces with the environment and are constitutively challenged by environmental stressors such as injury or pathogens (Sonnenberg et al., 2011; Zhang et al., 2022). Immune cells in barrier tissues must respond rapidly to environmental challenges and produce appropriate effector factors to maintain tissue homeostasis, promote tissue repair, or inhibit pathogen infection. Turning these immune effectors on and off through posttranscriptional mechanisms could be more efficient and economical than generating new transcripts. A recent study demonstrated, for example, that skin-resident Th17 and Tc17 cells were capable of constitutively expressing mRNA of type 2 cytokines (IL-5 and IL-13) without protein translation during homeostasis, causing them to respond quickly to intradermal chitin injection or insect exposure by producing type 2 cytokines (Harrison et al., 2019). Similarly, as intestinal sentinels, ILC3s could also rapidly respond to environmental signals, but without clear mechanisms (Guo et al., 2014; Mao et al., 2018; Zeng et al., 2019). Here, we find that ILC3s preserve mature cytokine mRNA in the nucleus through eIF6 blocking Nsun2-mediated mRNA m^5C modification at steady state, and after stimulation, activated p38α signaling can phosphorylate eIF6 and promote Nsun2-mediated mRNA m^5C modification, leading to nuclear export of cytokine mRNA and rapid cytokine production. The posttranscriptional regulation of cytokine production includes mRNA quality control, subcellular localization, decay, and translation of transcripts. Previous studies have shown that activation of the p38MAPK–MK2 pathway could phosphorylate and inhibit TTP, an RNA binding protein (RBP) that targets and delivers adenine and uridine–rich element (ARE)-containing transcripts to decay machinery (processing bodies, P-bodies), which results in the stabilization of mRNA and the production of proinflammatory cytokines such as TNFα in macrophage (Ronkina et al., 2019; Stoecklin et al., 2004; Tiedje et al., 2012). In contrast, our data suggest that activation of the p38MAPK pathway could promote mRNA nuclear export by regulating mRNA epigenetic modification in ILC3s. Further studies are needed to determine whether this mechanism is also present in other immune cells as well as non-immune cells. We also found that p38α deficiency in ILC2s and ILC1s led to decreased production of IL-5 and IFNγ at both RNA and protein levels, which is different from ILC3s, suggesting other mechanisms may be involved in p38α regulating ILC1s and ILC2s. Whether eIF6/Nsun2 pathway influences ILC1s and ILC2s needs further examination.

TL1A has previously been reported to activate p38α signaling and control ILC3 cytokine production (Castellanos et al., 2018; Li et al., 2019). We also noticed that TL1A could slightly activate p38α signaling in ILC3s, although much weaker than IL-1β. Interestingly, TL1A exhibits opposite effects in different colitis models, which may be attributed to the different intensities of p38 activation or different accompanying signals by different stimuli. Further investigation is still required to dissect the exact contribution of different stimuli to p38 activation in ILC3s in both homeostatic and inflammatory intestinal environments in vivo.

In addition to being involved in 60S ribosomal subunit biogenesis in the nucleus, eIF6 is also involved in ribosomal maturation and protein translation in the cytoplasm (Basu et al., 2001; Gandin et al., 2008; Weis et al., 2015). Here, our findings demonstrate that eIF6 influences nuclear retention or export of cytokine mRNA in ILC3s by regulating methyltransferase activity of Nsun2. It has been shown that premature mRNA with

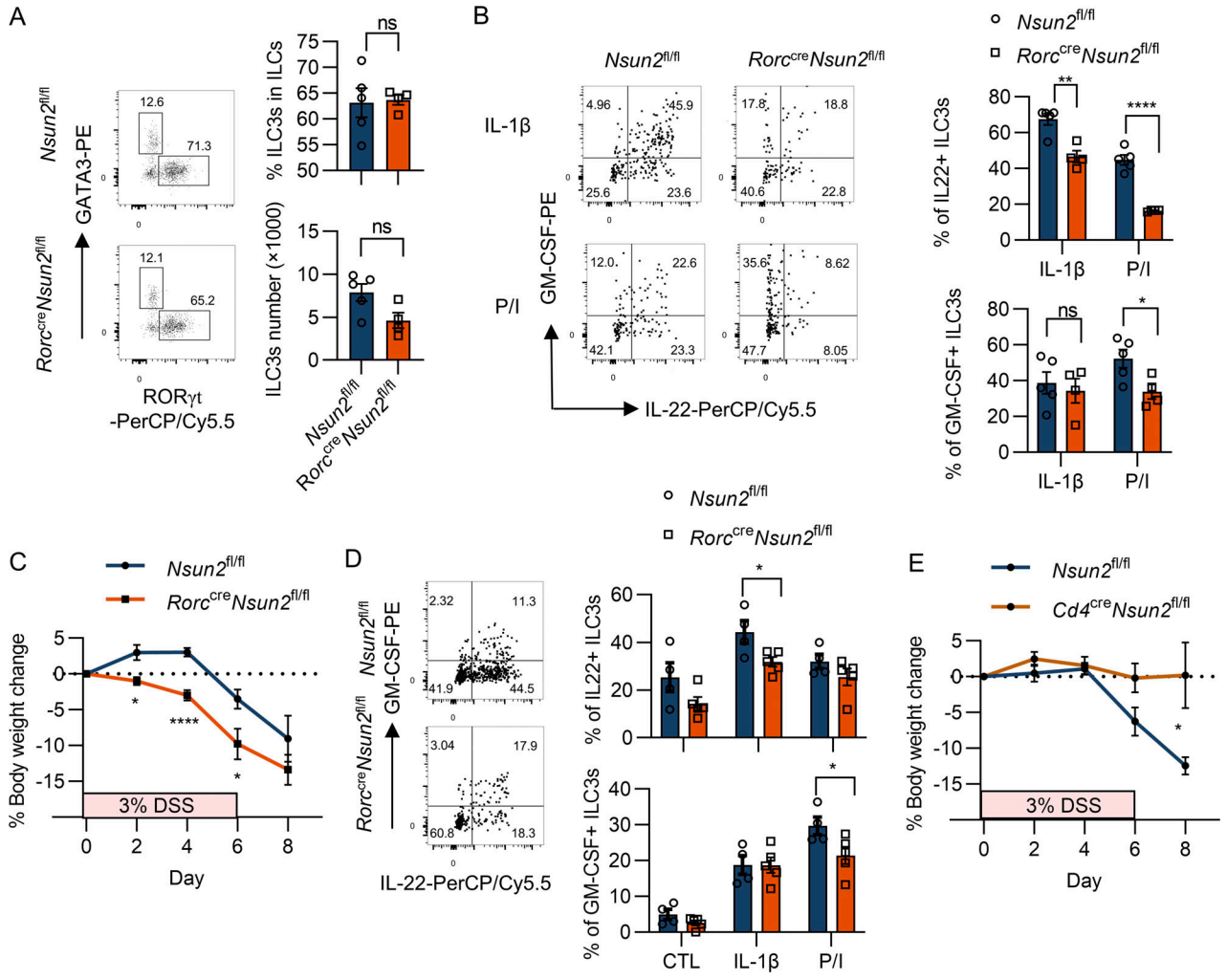

Figure 6. **Nsun2 in ILC3s is required for the cytokine production and host protection against colitis. (A)** ILC3s (gated in CD45$^+$CD90$^+$CD3$^-$RORγt$^+$) were isolated from colonic LPLs of *Nsun2*$^{fl/fl}$ (n = 5) and *Rorc*^{cre}*Nsun2*$^{fl/fl}$ (n = 4) mice and analyzed by flow cytometry. The percentages and absolute numbers of ILC3s are shown. **(B)** LPLs from colonic lamina propria of *Rorc*^{cre}*Nsun2*$^{fl/fl}$ (n = 4) or *Nsun2*$^{fl/fl}$ (n = 5) littermate mice were stimulated ex vivo with IL-1β or PMA/ionomycin (P/I). Representative flow cytometry and analysis of IL-22 and GM-CSF production by ILC3s (gating in eflour780$^-$CD45^{low}CD90$^+$ RORγt$^+$). **(C)** 8-wk-old *Rorc*^{cre}*Nsun2*$^{fl/fl}$ (n = 7) and their littermates *Nsun2*$^{fl/fl}$ (n = 8) were given 3% DSS in drinking water for 6 days. Body weight change curves were shown. Data are pooled from two independent experiments. **(D)** The IL-22 and GM-CSF production by ILC3s (gating in CD45$^+$CD90$^+$TCRβ$^-$RORγt$^+$) from *Rorc*^{cre}*Nsun2*$^{fl/fl}$ (n = 5) or *Nsun2*$^{fl/fl}$ (n = 4) mice at day 3 after DSS exposure. **(E)** 8-wk-old *Cd4*^{cre}*Nsun2*$^{fl/fl}$ (n = 3) and their littermates *Nsun2*$^{fl/fl}$ (n = 4) were given 3% DSS in drinking water for 6 days. Body weight change curves were shown. Data are representative of one of two independent experiments (A–E). Each dot (A, B, and D) represents one individual mouse. Data are mean ± SEM and statistical significance was tested by two-tailed Student's unpaired t test (A–E), *P < 0.05, **P < 0.01, ****P < 0.0001; ns, no significant difference.

retained introns could be stored in the nucleus (Wegener and Muller-McNicoll, 2018), whereas most mature mRNA is stored in the cytosol, such as stress granules (Molliex et al., 2015). Our data show that mature cytokine mRNA may aggregate with eIF6 and be preserved in the ILC3 nucleus. It would be intriguing to determine whether these transcripts retained in the nucleus have extended half-lives, and after activation of p38α signaling, these mature cytokine transcripts may be coupled with eIF6 and 60S ribosomal subunit in the nucleus and shuttle to the cytosol where they rapidly form translation machinery and generate cytokines, which is yet to be verified. Interestingly, we also notice that eIF6/Nsun2/mRNA forms speckle-like structures in the nucleus. Since liquid–liquid phase separation (LLPS) has emerged as a key mechanism underlying the formation of membrane-less organelles (Uversky, 2017), such as G3BP1, which can trigger phase separation to assemble stress granules (Alberti and Hyman, 2021; Marcelo et al., 2021), it is important to test whether LLPS can also be involved in the formation of eIF6/mRNA puncta in the ILC3 nucleus. Additionally, we find that the 3′UTRs of *Il22/Csf2* mRNA contain cis-elements that affect their nuclear retention. It would be worthwhile to further explore how eIF6 interacts with these 3′UTRs, whether it is sequence-specific, if other transcripts in ILC3s could be regulated by the same mechanism, and whether other immune cells share a similar posttranscriptional mechanism that regulates the expression of other cytokines.

It is well known that Nsun2 serves as a cytosine methylation enzyme mediating nuclear RNA shuttling to the cytosol (Yang

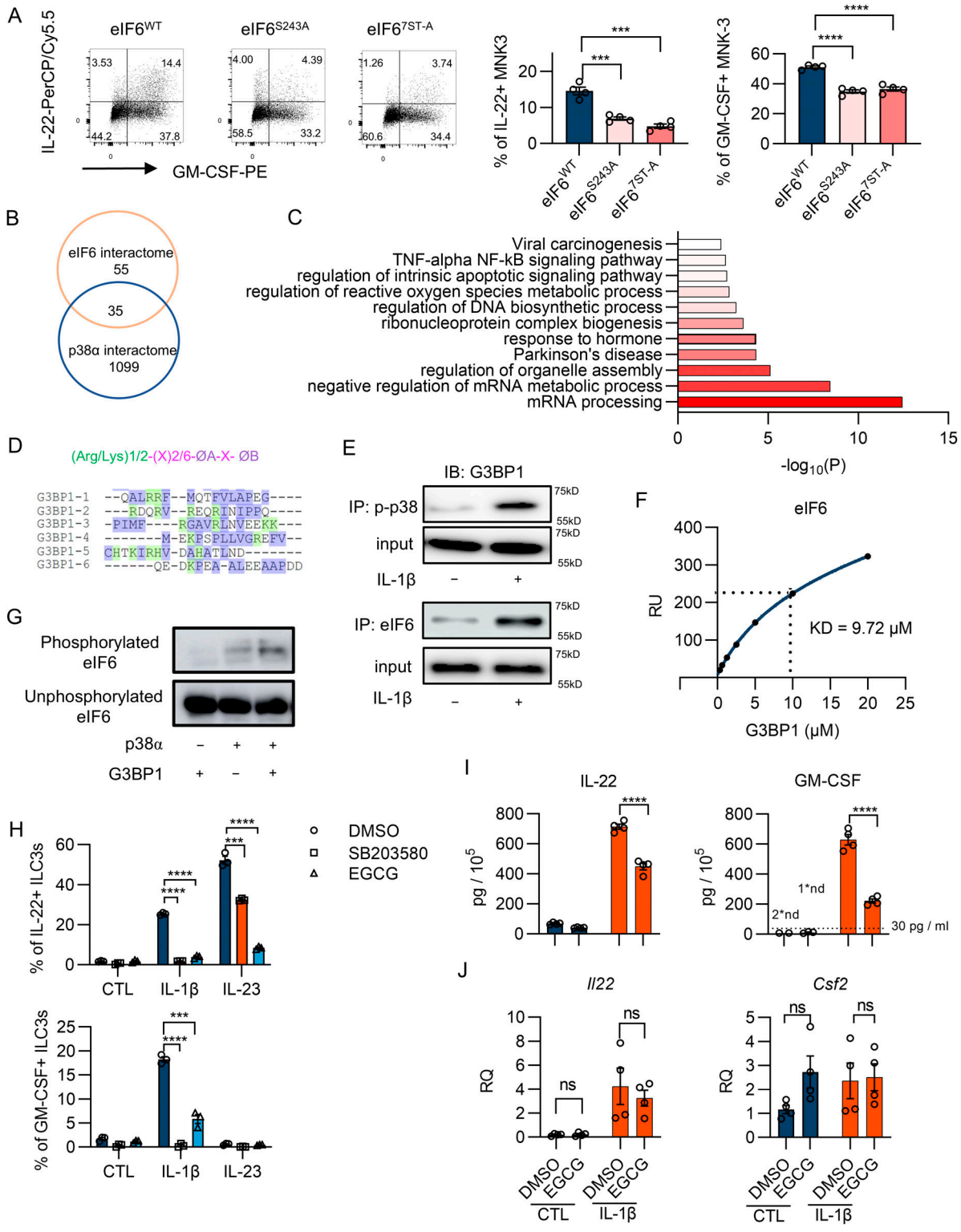

Figure 7. **G3BP1 assists p38α in phosphorylating eIF6 and promotes ILC3 immune response. (A)** MNK-3 cells were overexpressed with eIF6^{WT} or mutant eIF6 (eIF6^{S243A} and eIF6^{7ST-A}). The IL-22 and GM-CSF production was analyzed by flow cytometry. **(B and C)** eIF6-interactome were determined by immunoprecipitation with anti-eIF6 antibody followed by MS in ILC3s. **(B)** The Venn diagram shows the interactive analysis with the eIF6-interactome and TurboID-p38α-interactome. **(C)** The GO enrichment analysis of 35 proteins interacted with both eIF6 and p38α. **(D)** The p38α docking sequences in G3BP1. **(E)** Western blot analysis of the co-IP between p-p38α and G3BP1 or between eIF6 and G3BP in MNK-3 cells treated with or without IL-1β. **(F)** The binding affinity between G3BP1 and eIF6 (fixed phase) was measured by Biacore SPR assay. **(G)** eIF6 was incubated with p38α kinase buffer with or without G3BP1 protein in vitro. Western blot analysis of phosphorylated eIF6 following the kinase assay and Phos-tag SDS-PAGE. **(H)** The small intestine and colon LPLs from WT mice were pre-treated with EGCG and then stimulated with IL-1β or IL-23 for 4 h. The expression of IL-22 and GM-CSF in ILC3s (gated in eflour780^{-}CD45^{low}CD90^{high}) were analyzed by flow cytometry. **(I and J)** ILC3s sorted from the small intestine and colon LPLs of *Rag1*$^{-/-}$ mice were stimulated with IL-1β with or without

EGCG for 18 h. The protein (I) and mRNA (J) expression levels of IL-22 and GM-CSF were examined by ELISA and qPCR. Data are representative of one of two independent experiments (A and E–J). Each dot (A and H–J) represents one biological replicate; Biacore Insight Evaluation software (GE Healthcare) is applied to calculated the KD (F). Data are mean ± SEM and statistical significance was tested by two-tailed Student's unpaired *t* test (B and K), ***P < 0.001, ****P < 0.0001; ns, no significant difference. Source data are available for this figure: SourceData F7.

et al., 2017). Deletion of *Nsun2* in T cells may attenuate colitis by decreasing the half-life of *Il17a/f* mRNA in Th17 cells (Yang et al., 2017). We found that eIF6 inhibited Nsun2 methyltransferase activity by blocking SAM binding to Nsun2, and Nsun2 deficiency in ILC3s impaired IL-22 and GM-CSF production and aggravated colitis. Since T cells can also produce IL-22 (Sun et al., 2023), it is interesting to test whether the eIF6/Nsun2 axis also regulates T cell responses. Besides condensing untranslated mRNA and assembling stress granules, a recent study also showed that G3BP1 can activate cGAS enzymes to generate cGAMP (Liu et al., 2019). Our study shows that G3BP1 could facilitate p38α-mediated phosphorylation of eIF6, which should happen in the nucleus. As most G3BP1 protein is in the cytoplasm, it needs to determine whether and how G3BP1 enters the nucleus in response to IL-1β stimulation. Additionally, the G3BP1 inhibitor EGCG, enriched in green tea, has shown different effects in IBD models, either reducing inflammatory cytokine production and colon inflammation (Barbalho et al., 2019; Oz et al., 2013; Rahman et al., 2018) or accelerating weight loss in a DSS-induced colitis model (Oz et al., 2013). Our data showed that EGCG could suppress cytokines production in ILC3s in vitro. Whether ILC3s are involved in the effects of EGCG or green tea on intestinal inflammation in vivo requires further investigation.

In this study, we identified the unique role of p38α in ILC3s in maintaining intestinal mucosal homeostasis. At an older age, ILC3-specific p38α-deficient mice developed a spontaneous colon inflammation. Since the microbiome plays an important role in the development of IBD, and ILC3s are well known as a microbiota regulator, it may be interesting to investigate if the microbiome also contributes to spontaneous colitis in p38α-deficient mice. Additionally, p38α is also activated in DCs and macrophages in colitis. p38α deficiency in cDC1s could lead to increased IL-27 production through the TAK1–MKK4/7–JNK signaling pathway, further promoting IL-10 production by Tr1 cells and protecting mice from DSS-induced colitis (Zheng et al., 2018). Macrophage-specific deletion of p38α also exhibited attenuated colitis (Chen et al., 2022; Zhao et al., 2022). These data indicate that p38α in DCs and macrophages may promote IBD progression. In contrast, our data reveal that p38α regulates ILC3s' cytokine production and is crucial for restricting excessive inflammatory responses during colitis. Notably, p38α in ILC3s plays a vital role in maintaining gut homeostasis. ILC3-specific p38α deletion mice develop spontaneous colitis, indicating that dysfunction of ILC3s in response to daily stress could trigger inflammation. Thus, the contradictory roles of p38α in gut inflammatory disorders in mouse models might reflect its different effects in different types of cells (Coskun et al., 2011; ten Hove et al., 2002). Consistently, a recent clinical trial of p38 inhibitors for IBD also failed, suggesting that targeting p38α without cell specificity may not yield expected clinical outcomes in IBD (Coskun et al., 2011). Cell-specific inhibitors or agonists of p38MAPK should be developed and tested in the future.

In conclusion, our study identifies a novel pathway, the p38α–eIF6–Nsun2 axis, that regulates the nuclear export of cytokine mRNA in ILC3s. This strategy allows ILC3s to rapidly translate poised cytokine transcripts, thus protecting the host from intestinal inflammation by responding to environmental stress efficiently and economically.

Materials and methods

Mice

The different strains of mice used were bred and kept in specific pathogen-free facilities at the Animal Center of Tsinghua University. The strains of mice include C57BL/6, *Rag1*$^{-/-}$, *Rorc*$^{gfp/+}$, *Mapk14*$^{fl/fl}$, *Rorc*^{Cre}*Mapk14*$^{fl/fl}$, *Cd4*^{Cre}*Mapk14*$^{fl/fl}$, *Vavi*^{Cre}*Mapk14*$^{fl/fl}$, *Nsun2* $^{fl/fl}$, and *Rorc*^{Cre}*Nsun2*$^{fl/fl}$. *Rorc*^{cre} (Eberl and Littman, 2004) and *Rorc*$^{gfp/+}$ (Eberl et al., 2004) mice were from Dan R. Littman (New York University, New York, NY, USA); *Vavi*^{Cre} (Ogilvy et al., 1998) were from Li Wu (Tsinghua University, Beijing, China); *Mapk14*$^{fl/fl}$ (Kang et al., 2008) were from Jiahuai Han (Xiamen University, Xiamen, China); *Nsun2*$^{fl/fl}$ (Yang et al., 2017) were from Yun-Gui Yang (Institute of Genomics, Beijing, China) and Zhong-Zhou Yang (Nanjing University Medical School, Nanjing, China); *Cd4*^{cre} (Lee et al., 2001) were purchased from Taconic; and *Rag1*$^{-/-}$ mice were purchased from Jackson Laboratory. All experiments were conducted with sex- and age-matched. All animal experiments and protocols were performed according to Tsinghua animal care committees' procedures.

DSS-induced acute colitis

To setup the colitis model in mice, the chemical inducer DSS was administrated to 8–12-wk-old sex-matched mice. In brief, DSS-induced colitis was induced by administrating 3% (wt/vol) DSS (0216011080; MP) in drinking water for 6 days and then the drinking water was switched to normal water. During this period, the body weight was measured every other day and the mice were sacrificed on the indicated day. The colons were collected for immunofluorescence analysis, flow cytometry, qPCR, and histology analysis.

Isolation of colonic lymphocytes

Intestines were cut open longitudinally and cut into 1.5-cm pieces, washed in 1× PBS by vortex, and shaken in Buffer I (HBSS containing 1 mM DTT (D0632; Sigma-Aldrich), 5 mM EDTA, 3% FBS, and 10 mM HEPES) at 37°C for 20 min twice. After Buffer I, the tissue was further washed in Buffer II (HBSS containing 10 mM HEPES) for 20 min and the tissues were then digested in RPMI 1640 medium containing 0.05% DNase I (DN25; Sigma-Aldrich) and 0.1 mg/ml Liberase (05401020001; Roche) at 37°C

for 20–30 min. Then the digested tissues were homogenized by gentleMACS Dissociator (Miltenyi) and passed through a 70-µm cell strainer. Mononuclear cells were harvested from the interphase of an 80% and 40% Percoll gradient after a spin at 2,000 rpm for 20 min at 4°C without break.

Flow cytometry analysis

Cells were stained for viability using the Fixable Viability Dye eFluor 780 (65-0865-14; eBioscience), followed by surface staining with varying combinations of the following antibodies in FACS buffer (1× PBS + 2% FBS + 0.02% NaN_3): CD45 (clone 30-F11, 103128; BioLegend), CD3 (clone 145-2C11, 100320; BioLegend), CD90.2 (clone 30-H12, 105335; BioLegend), CD4 (clone GK1.5, 63-0041-82; eBioscience), and TCRβ (clone H57-597, 109206; BioLegend). For the intracellular cytokine staining, cells were ex vivo–stimulated with indicated stimulators for 4 h, and Brefeldin A (HY-16592; MCE) was added to block the secretion of cytokines for 3 h. Cells were fixed with IC Fixation Buffer (00-8222-49; eBioscience), and then cells were stained with IL-17A (clone eBio17B7, 17-7177-81; eBioscience), IL-22 (clone IL22JOP, 46-7222-82; eBioscience), IFNγ (clone XMG1.2, 48-7311-82; eBioscience), and GM-CSF (clone BVD2-21C11, 554406; BD). For transcription factor staining, cells were fixed and permeabilized using Foxp3/Transcription Factor Fixation/Permeabilization Concentrate and Diluent (00-5523-00; eBioscience), and intracellular staining was performed for Foxp3 (clone FjK-16s, 17-5773-82; Invitrogen), RORγt (clone B2D, 25-6981-80; eBioscience), GATA-3 (clone TWAJ, 50-9966-42; Thermo Fisher Scientific), and respective manufacturer isotype control antibodies. Flow cytometry was performed on Fortessa instruments (BD Biosciences) and analyzed with FlowJo software (V10).

Immunofluorescence staining and confocal imaging

The protocol was according to a previous report (Mao et al., 2018). In brief, the colon was excised after a 3-day DSS treatment, and the Swiss roll was prepared and incubated in a fixation buffer (00-5223-56; BioLegend) overnight. The fixed tissue was dehydrated in 30% sucrose for at least 6 h and embedded in OCT compound (4583; Sakura), which would be moved into −80°C fridge. Sections of 15-µm thickness were cut on CM3050 S Cryostat (Leica) and adhered to slides. Before the markers staining procedure, the slides were fixed again in methanol for 20 min at −20°C and permeabilized in PBS containing 0.3% Triton X-100 and then blocked in PBS containing 10% fetal bovine serum (blocking buffer) for 1 h. For the markers staining, the antibodies were diluted in a blocking buffer and then the sections were incubated in the buffer overnight. After antibody staining, the slides were mounted with Flourmount G (00-4958-02; Thermo Fisher Scientific), and then the image data were collected on Zeiss LSM880 with Airyscan. The antibodies were used for staining: anti-CD45 (clone 104, 109808; Biolegend), anti-EpCAM (clone RTK2758, 400532; BioLegend), anti-p-p38 (clone D3F9, 4511S; CST), and anti-GFP (clone FM264G, 338007; BioLegend).

Histological assessment of colon tissue

Colons were collected from mice and the Swiss roll was prepared. The fixed tissue was paraffin-embedded and 4-µm sections were used for H&E staining. Embedding, sectioning, and H&E staining services were provided by Laboratory Animal Resources Center, University. A blind evaluation of colitis severity was assessed by a combined score of colon cellular infiltration (0–4, according to the number and localization of the inflammatory cells), tissue disruption (0–4, according to the severity of mucosal and crypts damages), and tertiary lymphoid structures formation (0–4, according to the numbers), as described previously (Erben et al., 2014).

Cell culture

293T cells were grown in DMEM supplemented with 10% fetal bovine serum, sodium pyruvate, and penicillin/streptomycin (15140122; Thermo Fisher Scientific) at 37°C, 5% CO_2. For the ILC3′ cytokine expression assay in 293T cells, the cells were grown in a 24-well plate. When the confluency was up to 70–80%, the transfection was performed with indicated vectors via lipo3000 (L3000015; Thermo Fisher Scientific) according to the manufacturer's instructions. The supernatant was collected at 24 and 48 h for ELISA detection of IL-22 (436304; BioLegend) and GM-CSF (432207; BioLegend). For the MNK-3 cell line culture, the culture protocol was according to a previous report (Allan et al., 2015). In short, the MNK-3 cells were cultured in DMEM with 10% fetal bovine serum, 2 mM GlutaMAX, 1 mM sodium pyruvate, 55 µM 2-mercaptoethanol, 10 mM HEPES, and 100 µg/ml penicillin and streptomycin. To maintain the property of MNK-3 cells, 10 ng/ml IL-7, 10 ng/ml IL-15, and 10 ng/ml retinoic acid were added to the culture medium. To generate eIF6-overexpressing or eIF6-knocking-down MNK-3 cell lines, the indicated viral supernatants were prepared from Plat-E packaging cells, and MNK-3 cells were infected, and then the GFP^+ MNK-3 cells were sorted by flow cytometry.

Biotin labeling with p38α-TurboID in MNK-3 cells

p38α interactome in MNK-3 cells was identified by the TurboID system according to the protocol from Alice Ting's lab (Branon et al., 2018). In brief, *Mapk14* and Turbo were fused into MigR1 plasmid and then the retrovirus was packaged. MNK-3 cells were infected by the retrovirus, and after 48 h infection, the cells were treated with IL-1β with biotin addition for 2 h. Labeling was stopped on ice and washed five times with ice-cold PBS. The pellets were lysed by cell lysis buffer (25 mM HEPES, 150 mM NaCl, 1% Triton) and the biotinylated proteins were enriched by streptavidin beads for 1 h at room temperature and then moved to 4°C and incubated overnight with rotation. The beads were subsequently washed according to the protocol and then boiled in protein loading buffer supplemented with 20 mM DTT. The eluate was then separated on SDS-PAGE gel and the total lane was collected for MS detection. The MS results were analyzed by GO through Metascape (Zhou et al., 2019).

smFISH

MNK-3 cells were cultured in µ-Slide 8 Well high (80806; ibidi), and the probes were designed according to Biosearch Technologies. Stellaris RNA fluorescence in situ hybridization (FISH). All probe sets were manufactured by XianghongBio, and the *Il22/Csf2* was labeled with TAMRA. Cells were fixed with RNAse-free 4% paraformaldehyde for 20 min and washed with PBS

twice. The cells were permeabilized in 70% ethanol overnight at 4°C. The cells were hybridized with combinations of probe sets overnight at 37°C and washed with wash buffer (10% 20×SSC, 10% formamide in DEPC water) five times (the third wash was in 37°C incubator for 30 min) and then processed by immunofluorescence procedures for eIF6 (clone A-2, sc-390432; Santa Cruz) and Nsun2 (20854-1-AP; Proteintech) staining. The cells were imaged by ZEISS LSM 980 with Airyscan 2.

Immunoprecipitation

For immunoprecipitation of eIF6 and p-p38, lysates with 500 µg of total protein were suspended in a final volume of 500 µl of CLB supplemented with protease and phosphatase inhibitors. The lysates were incubated with anti-eIF6 (clone A-2, sc-390432; Santa Cruz) or anti-p-p38 (clone D3F9, 4511; CST) overnight at 4°C. The protein A/G magnetic beads (HY-K0202; MCE) were precleared with CLB and the buffer and beads were separated by a magnetic separator. Precleared beads were incubated with lysate mix and rotated for 1 h at 4°C. The samples were washed five times in CLB buffer, and the beads were collected by magnetic separator. The beads were boiled with protein loading buffer at 100°C for 10 min.

Quantitative real-time PCR

Total RNA of tissues or cells was isolated using the Trizol manufacturer, and cDNA was prepared using the RevertAid First Strand cDNA Synthesis Kit (Thermo Fisher Scientific). Real-time PCR was performed with the real-time PCR StepOnePlus system (Applied Biosystems) using Hieff qPCR SYBR Green Master Mix (11203ES08; Yeasen). Data were normalized to *Hprt* or *Actb* and analyzed by the $2^{-\Delta\Delta CT}$ method. The sequence of qPCR primers is shown in the Table S6.

Identification of the RBP binding to ILC3 cytokine's mRNA-3′UTR

The procedures for identifying the RBP followed the Myriam Gorospe protocol (Panda et al., 2016). In brief, the biotinylated *Il22*-CDS and *Il22*-CDS+3′UTR were generated in vitro via MEGAlongtcript T7 kit (AM1345; Thermo Fisher Scientific), additionally adding 3′-Biotin guanosine triphosphate (GTP) (N0760S; NEB) following the manufacturer's protocol. For the preparation of ILC3 lysate, the sorted ILC3s from the gut were stimulated with or without IL-1β for 1 h and then the cells were disrupted by polysome extraction buffer (PEB). There were four groups that needed 2 million ILC3 cells for each biotinylated RNA, and the lysate combination with biotinylated RNA was incubated for 30 min. After incubation, the 50 µl streptavidin-conjugated Dynabeads were added into each reaction for 30 min and then beads were washed three times with TENT buffer. The beads were boiled in a protein loading buffer and the buffers were loaded on SDS-PAGE gel, and after PAGE finishing, the gel was sent to MS to identify specific proteins.

Plasmids

cDNA encoding *Il22*, *Csf2*, and *Eif6* and its related mutants were subcloned into pEGFPn1 or 3xFlag-N-CMV, and different versions of *Eif6* were subcloned into MigR1 for generating retrovirus. For prokaryotic protein expression in *Escherichia coli* (*E. coli*), cDNA encoding *Eif6* related mutants and *G3bp1* were subcloned into pGEX6p1 and cDNA encoding *Mapk14* and *Nsun2* was subcloned into pET28a. For shRNA vector, shRNA-containing oligonucleotides for *Eif6* (the sequence: 5′-TGCTGT TGACAGTGAGCGCAG CTACTGTGTCTTCAGTAATTAGTGAAG CCACAGATGTAATTACTGAAGACACAGTAGCTTTGCCTACTG CCTCGGA-3′) were cloned into the plasmid pLMP-Ametrine.

Expression and purification of p38α, eIF6, G3BP1, and Nsun2

For the pGEX6p1 protein expression and purification system, eIF6 and G3BP1 were expressed and purified from *E. coli* Rosetta 2(DE3) cells. A TEV cleaved site between GST and the target was introduced into these constructs. Upon OD600 of *E.coli* reaching 0.8, 0.5 mM IPTG was added at 16°C overnight. The cells were collected and suspended in PBS for homogenizing by ultrahigh-pressure homogenizer. After homogenization, the cell lysate pelleted at 30,000 × *g* at 4°C for 30 min. The supernatant was incubated with packed GST columns (Cytiva) as provided by the manufacturer. Proteins were eluted with 10 mM glutathione, and the eluent was incubated with TEV protease at 4°C overnight. The cleaved protein was further purified by ion exchange with a Q column (GE) and Superdex 200 16/200 column (GE). The fractions were determined by SDS-PAGE, pooled, concentrated, filtered, flash-frozen in liquid nitrogen, and stored at −80°C. For pET28a protein expression and purification system, the majority of the procedure was similar to pGEX6p1. The optimal induction temperature is different. For p38α purification, the optimal temperature is 30°C while 37°C is optimal for Nsun2 for 4 h.

p38α kinase assay

All protein components were purified according to previous steps, and the MKK6EE was purchased from SinoBiological (10422-H20B1-20). The assay was performed in a final volume of 20 µl of kinase buffer. The activator (0.5 µg MKK6EE), 1 µg p38α, the substrate (5 µg eIF6), and 250 µM ATP with or without G3BP1 were incubated in kinase buffer (9802; CST) at 30°Cfor 30 min. After kinase incubation, the protein loading buffer was added and then boiled. The phos-tag PAGE (198-17981; WAKO) was applied to separate the phosphorylated and unphosphorylated eIF6 for MS and western blot detection.

In vitro Nsun2-mediated m^{5}C modification assay

The *Il22/Csf2* mRNA substrates were transcribed in vitro. In vitro methylation assay was performed at 37°C for 2 h in 50 µl of reaction mixture consisting of 20 mM HEPES-KOH (pH 8.0), 5 mM $MgCl_2$, 100 mM KCl, 1 mM DTT, 1 µg *Il22/Csf2* transcript, 0.5 µM Nsun2, and 1 mM *S*-adenosylmethionine (SAM) in the presence or absence of eIF6. After the reaction, the mRNA was purified according to the Monarch RNA Cleanup Kit (T2030L; NEB), and the purified mRNA was digested by Nucleoside Digestion Mix (M0649S; NEB). The samples were subjected to LC/MS analysis.

m^{5}C Dot blot assay

The total RNA was extracted from MNK-3 cells. The mRNA samples were quantified by Nanodrop (Thermo Fisher Scientific). For the dot blot assay, equal amounts of RNA were loaded on the positively charged nylon transfer membrane (GE

Healthcare). After 254 nm UV crosslinking for 30 min, the membrane was blocked with 5% non-fat milk in PBS with 0.1% Tween-20 (PBST), followed by incubation with the primary rabbit anti-m^{5}C antibody (clone D3S2Z, 28692S; CST) and then peroxidase goat anti-Rabbit IgG (H+L) (A0208; Beyotime) secondary antibody. m^{5}C RNA levels were visualized by enhanced chemiluminescence (Millipore). Equal RNA loading was verified by methylene blue (G1300; Solarbio) staining.

Binding kinetics measured by Biacore SPR assay

The binding kinetics were analyzed by SPR (Biacore 8k+; Cytiva). The indicated analyst was immobilized to a sensor chip CM5 via amine groups in 10 mM sodium acetate buffer (pH 4.0 for eIF6 and p38α and pH 5.0 for Nsun2) for a final RU around 80000. The running buffer was composed of PBST (0.05% Tween-20). For kinetics analyte, the concentrations of SAM ranging from 0.03125 to 3 μM, eIF6 from 0.78125 to 12.5 μM, Nsun2 from 0.06 to 5 μM, or indicated conditions flowed over the chip at a flow rate of 30 μl/min for 60s, followed by 180s dissociation. The data were fitted to a 1:1 binding model using Biacore Insight Evaluation software (Cytiva).

Statistical analysis

Data were analyzed on GraphPad Prism 9 (GraphPad Software). A two-tailed unpaired Student's *t* test was used for comparison between the two groups. The log-rank (Mantel–Cox) test were used for survival statistical analysis. Dissociation-one phase decay is applied to fit KD. Data are presented as mean values ± SEM; $P < 0.05$ was considered significant. Given that mouse experiments required littermate controls and complex genotyping, experimental group allocation was not blinded.

Online supplemental material

Fig. S1 illustrates the activation patterns of p38, ERK, and JNK in immune and epithelial cells during both naïve and inflammatory states. Fig. S2 analyses the regulatory role of *Mapkl4* in the development and function of ILC3 subsets, as well as cytokine production by other ILCs. Fig. S3 displays the strategic experiments validating the IL-1β–p38α axis-mediated posttranscriptional mechanisms. Fig. S4 provides an analysis of ILC3 cytokines and the expression of *Il1r1*, *Il1r2*, and *Dusp1* in *Nsun2*$^{fl/fl}$ and *Rorc*^{cre}*Nsun2*$^{fl/fl}$ mice. Fig. S5 examines the potential phosphorylation of eIF6 by MAPKs and GSK3β, along with MS results for the phosphorylated sites of eIF6 by p38α. Table S1 shows the p38α-TurboID interactome. Table S2 displays the differential analysis of p38α interactome. Table S3 shows the *Il22* mRNA interactome. Table S4 displays the eIF6 interactome in ILC3s. Table S5 exhibits the components in both eIF6 and p38α interactome. Table S6 shows the sequence of qPCR primers.

Data availability

The data are available in the main article, the supplemental materials, and the source data file.

Acknowledgments

We thank all members of Xiaohuan Guo's lab for the helpful discussion. We are grateful to Dan R. Littman and Ivaylo Ivanov (New York University, New York, NY, USA) for *Rorc*^{cre} and *Rorc*$^{gfp/+}$mice; Yun-Gui Yang (Institute of Genomics, Beijing, China) and Zhong-Zhou Yang (Nanjing University Medical School, Nanjing, China) for *Nsun2*$^{fl/fl}$ mice; James R. Carlyle (University of Toronto, Toronto, Canada) and David S.J. Allan (National Heart, Lung, and Blood Institute, National Institutes of Health, Bethesda, MD, USA) for MNK-3 cells; Peng Zou (Peking University, Beijing, China) for Turbo plasmids; Yuanyuan Li (Tsinghua University, Beijing, China) for helpful suggestion. We also thank the Core Facility of the Institute for Immunology and the Animal Facility at Tsinghua University for their support.

This work was supported by the National Natural Science Foundation of China (82150104, 82122030, 32170872, 82141201, and 31821003 to X. Guo; 82388101 and 31991174 to L. Wu), the National Key R&D Program of China (2023YFC2306202 and 2017YFA0103602 to X. Guo), Beijing Natural Science Foundation (Z210015 to X. Guo), the National Key Research Program, Ministry of Science and Technology of China (2019YFA0508502, 2020YFC2505001 to L. Wu). The Guo laboratory was also supported by the Shanxi Medical University (SXMU)-Tsinghua Collaborative Innovation Center for Frontier Medicine and the Institute for Immunology, Tsinghua University.

Author contributions: Jida Huang: Conceptualization, Data curation, Formal analysis, Investigation, Methodology, Project administration, Validation, Visualization, Writing - original draft, Writing - review & editing, J. Zhang: Investigation, P. Song: Investigation, Jiaoyan Huang: Investigation, Z. Yang: Investigation, J. Han: Resources, L. Wu: Conceptualization, Funding acquisition, Supervision, X. Guo: Conceptualization, Data curation, Funding acquisition, Methodology, Project administration, Resources, Supervision, Visualization, Writing - original draft, Writing - review & editing.

Disclosures: The authors declare no competing interests exist.

Submitted: 8 April 2024
Revised: 1 September 2024
Accepted: 8 October 2024

References

Alberti, S., and A.A. Hyman. 2021. Biomolecular condensates at the nexus of cellular stress, protein aggregation disease and ageing. *Nat. Rev. Mol. Cell Biol.* 22:196–213. https://doi.org/10.1038/s41580-020-00326-6

Allan, D.S., C.L. Kirkham, O.A. Aguilar, L.C. Qu, P. Chen, J.H. Fine, P. Serra, G. Awong, J.L. Gommerman, J.C. Zúñiga-Pflücker, and J.R. Carlyle. 2015. An in vitro model of innate lymphoid cell function and differentiation. *Mucosal Immunol.* 8:340–351. https://doi.org/10.1038/mi.2014.71

Andreassi, C., and A. Riccio. 2009. To localize or not to localize: mRNA fate is in 3'UTR ends. *Trends Cell Biol.* 19:465–474. https://doi.org/10.1016/j.tcb.2009.06.001

Barbalho, S.M., H. Bosso, L.M. Salzedas-Pescinini, and R. de Alvares Goulart. 2019. Green tea: A possibility in the therapeutic approach of inflammatory bowel diseases?: Green tea and inflammatory bowel diseases. *Complement. Ther. Med.* 43:148–153. https://doi.org/10.1016/j.ctim.2019.01.015

Basu, U., K. Si, J.R. Warner, and U. Maitra. 2001. The Saccharomyces cerevisiae TIF6 gene encoding translation initiation factor 6 is required for 60S ribosomal subunit biogenesis. *Mol. Cell. Biol.* 21:1453–1462. https://doi.org/10.1128/MCB.21.5.1453-1462.2001

Branon, T.C., J.A. Bosch, A.D. Sanchez, N.D. Udeshi, T. Svinkina, S.A. Carr, J.L. Feldman, N. Perrimon, and A.Y. Ting. 2018. Efficient proximity labeling

in living cells and organisms with TurboID. *Nat. Biotechnol.* 36:880–887. https://doi.org/10.1038/nbt.4201

Castellanos, J.G., V. Woo, M. Viladomiu, G. Putzel, S. Lima, G.E. Diehl, A.R. Marderstein, J. Gandara, A.R. Perez, D.R. Withers, et al. 2018. Microbiota-induced TNF-like ligand 1A drives group 3 innate lymphoid cell-mediated barrier protection and intestinal T cell activation during colitis. *Immunity*. 49:1077–1089.e5. https://doi.org/10.1016/j.immuni.2018.10.014

Chen, W., R. Liang, Y. Yi, J. Zhu, and J. Zhang. 2022. P38α deficiency in macrophages ameliorates murine experimental colitis by regulating inflammation and immune process. *Pathol. Res. Pract.* 233:153881. https://doi.org/10.1016/j.prp.2022.153881

Coskun, M., J. Olsen, J.B. Seidelin, and O.H. Nielsen. 2011. MAP kinases in inflammatory bowel disease. *Clin. Chim. Acta*. 412:513–520. https://doi.org/10.1016/j.cca.2010.12.020

Eberl, G., and D.R. Littman. 2004. Thymic origin of intestinal αß T cells revealed by fate mapping of RORγt$^+$ cells. *Science*. 305:248–251. https://doi.org/10.1126/science.1096472

Eberl, G., S. Marmon, M.-J. Sunshine, P.D. Rennert, Y. Choi, and D.R. Littman. 2004. An essential function for the nuclear receptor RORgamma(t) in the generation of fetal lymphoid tissue inducer cells. *Nat. Immunol.* 5: 64–73. https://doi.org/10.1038/ni1022

Erben, U., C. Loddenkemper, K. Doerfel, S. Spieckermann, D. Haller, M.M. Heimesaat, M. Zeitz, B. Siegmund, and A.A. Kühl. 2014. A guide to histomorphological evaluation of intestinal inflammation in mouse models. *Int. J. Clin. Exp. Pathol.* 7:4557–4576.

Gandin, V., A. Miluzio, A.M. Barbieri, A. Beugnet, H. Kiyokawa, P.C. Marchisio, and S. Biffo. 2008. Eukaryotic initiation factor 6 is rate-limiting in translation, growth and transformation. *Nature*. 455: 684–688. https://doi.org/10.1038/nature07267

Goc, J., M. Lv, N.J. Bessman, A.L. Flamar, S. Sahota, H. Suzuki, F. Teng, G.G. Putzel, G. Eberl, D.R. Withers, et al. 2021. Dysregulation of ILC3s unleashes progression and immunotherapy resistance in colon cancer. *Cell*. 184:5015–5030.e16. https://doi.org/10.1016/j.cell.2021.07.029

Goldberg, R., N. Prescott, G.M. Lord, T.T. MacDonald, and N. Powell. 2015. The unusual suspects--innate lymphoid cells as novel therapeutic targets in IBD. *Nat. Rev. Gastroenterol. Hepatol.* 12:271–283. https://doi.org/10.1038/nrgastro.2015.52

Guo, X., J. Qiu, T. Tu, X. Yang, L. Deng, R.A. Anders, L. Zhou, and Y.X. Fu. 2014. Induction of innate lymphoid cell-derived interleukin-22 by the transcription factor STAT3 mediates protection against intestinal infection. *Infect. Immun.* 40:25–39. https://doi.org/10.1016/j.immuni.2013.10.021

Harrison, O.J., J.L. Linehan, H.Y. Shih, N. Bouladoux, S.J. Han, M. Smelkinson, S.K. Sen, A.L. Byrd, M. Enamorado, C. Yao, et al. 2019. Commensal-specific T cell plasticity promotes rapid tissue adaptation to injury. *Science*. 363:eaat6280. https://doi.org/10.1126/science.aat6280

Hu, Y., X. Liu, Y. Zhang, and X. Guo. 2023. The interaction network between group 3 innate lymphoid cells and other cells. *Fundam. Res.* https://doi.org/10.1016/j.fmre.2023.10.021

Huang, J., L. Fu, J. Huang, J. Zhao, X. Zhang, W. Wang, Y. Liu, B. Sun, J. Qiu, X. Hu, et al. 2022. Group 3 innate lymphoid cells protect the host from the uropathogenic Escherichia coli infection in the bladder. *Adv. Sci.* 9: e2103303. https://doi.org/10.1002/advs.202103303

Jungers, C.F., J.M. Elliff, D.S. Masson-Meyers, C.J. Phiel, and S. Origanti. 2020. Regulation of eukaryotic translation initiation factor 6 dynamics through multisite phosphorylation by GSK3. *J. Biol. Chem.* 295: 12796–12813. https://doi.org/10.1074/jbc.RA120.013324

Kang, Y.J., J. Chen, M. Otsuka, J. Mols, S. Ren, Y. Wang, and J. Han. 2008. Macrophage deletion of p38α partially impairs lipopolysaccharide-induced cellular activation. *J. Immunol.* 180:5075–5082. https://doi.org/10.4049/jimmunol.180.7.5075

Kaplan, G.G. 2015. The global burden of IBD: From 2015 to 2025. *Nat. Rev. Gastroenterol. Hepatol.* 12:720–727. https://doi.org/10.1038/nrgastro.2015.150

Lavelle, A., and H. Sokol. 2020. Gut microbiota-derived metabolites as key actors in inflammatory bowel disease. *Nat. Rev. Gastroenterol. Hepatol.* 17:223–237. https://doi.org/10.1038/s41575-019-0258-z

Lee, P.P., D.R. Fitzpatrick, C. Beard, H.K. Jessup, S. Jessup, S. Lehar, K.W. Makar, M. Pérez-Melgosa, M.T. Sweetser, M.S. Schlissel, et al. 2001. A critical role for Dnmt1 and DNA methylation in T cell development, function, and survival. *Immunity*. 15:763–774. https://doi.org/10.1016/s1074-7613(01)00227-8

Li, J., W. Shi, H. Sun, Y. Ji, Y. Chen, X. Guo, H. Sheng, J. Shu, L. Zhou, T. Cai, and J. Qiu. 2019. Activation of DR3 signaling causes loss of ILC3s and exacerbates intestinal inflammation. *Nat. Commun.* 10:3371. https://doi.org/10.1038/s41467-019-11304-8

Liu, Z.S., H. Cai, W. Xue, M. Wang, T. Xia, W.J. Li, J.Q. Xing, M. Zhao, Y.J. Huang, S. Chen, et al. 2019. G3BP1 promotes DNA binding and activation of cGAS. *Nat. Immunol.* 20:18–28. https://doi.org/10.1038/s41590-018-0262-4

Mao, K., A.P. Baptista, S. Tamoutounour, L. Zhuang, N. Bouladoux, A.J. Martins, Y. Huang, M.Y. Gerner, Y. Belkaid, and R.N. Germain. 2018. Innate and adaptive lymphocytes sequentially shape the gut microbiota and lipid metabolism. *Nature*. 554:255–259. https://doi.org/10.1038/nature25437

Marcelo, A., R. Koppenol, L.P. de Almeida, C.A. Matos, and C. Nóbrega. 2021. Stress granules, RNA-binding proteins and polyglutamine diseases: Too much aggregation? *Cell Death Dis.* 12:592. https://doi.org/10.1038/s41419-021-03873-8

Molliex, A., J. Temirov, J. Lee, M. Coughlin, A.P. Kanagaraj, H.J. Kim, T. Mittag, and J.P. Taylor. 2015. Phase separation by low complexity domains promotes stress granule assembly and drives pathological fibrillization. *Cell*. 163:123–133. https://doi.org/10.1016/j.cell.2015.09.015

Ogilvy, S., A.G. Elefanty, J. Visvader, M.L. Bath, A.W. Harris, and J.M. Adams. 1998. Transcriptional regulation of vav, a gene expressed throughout the hematopoietic compartment. *Blood*. 91:419–430.

Oz, H.S., T. Chen, and W.J.S. de Villiers. 2013. Green tea polyphenols and sulfasalazine have parallel anti-inflammatory properties in colitis models. *Front. Immunol.* 4:132. https://doi.org/10.3389/fimmu.2013.00132

Panda, A.C., J.L. Martindale, and M. Gorospe. 2016. Affinity pulldown of biotinylated RNA for detection of protein-RNA complexes. *Bio Protoc.* 6: e2062. https://doi.org/10.21769/BioProtoc.2062

Rahman, S.U., Y. Li, Y. Huang, L. Zhu, S. Feng, J. Wu, and X. Wang. 2018. Treatment of inflammatory bowel disease via green tea polyphenols: Possible application and protective approaches. *Inflammopharmacology*. 26:319–330. https://doi.org/10.1007/s10787-018-0462-4

Ronkina, N., N. Shushakova, C. Tiedje, T. Yakovleva, M.A.X. Tollenaere, A. Scott, T.S. Batth, J.V. Olsen, A. Helmke, S.H. Bekker-Jensen, et al. 2019. The role of TTP phosphorylation in the regulation of inflammatory cytokine production by MK2/3. *J. Immunol.* 203:2291–2300. https://doi.org/10.4049/jimmunol.1801221

Sonnenberg, G.F., L.A. Fouser, and D. Artis. 2011. Border patrol: Regulation of immunity, inflammation and tissue homeostasis at barrier surfaces by IL-22. *Nat. Immunol.* 12:383–390. https://doi.org/10.1038/ni.2025

Stoecklin, G., T. Stubbs, N. Kedersha, S. Wax, W.F. Rigby, T.K. Blackwell, and P. Anderson. 2004. MK2-induced tristetraprolin:14-3-3 complexes prevent stress granule association and ARE-mRNA decay. *EMBO J.* 23: 1313–1324. https://doi.org/10.1038/sj.emboj.7600163

Sun, L., Y. Su, A. Jiao, X. Wang, and B. Zhang. 2023. T cells in health and disease. *Signal Transduct. Target. Ther.* 8. 235. https://doi.org/10.1038/s41392-023-01471-y

ten Hove, T., B. van den Blink, I. Pronk, P. Drillenburg, M.P. Peppelenbosch, and S.J.H. van Deventer. 2002. Dichotomal role of inhibition of p38 MAPK with SB 203580 in experimental colitis. *Gut*. 50:507–512. https://doi.org/10.1136/gut.50.4.507

Tiedje, C., N. Ronkina, M. Tehrani, S. Dhamija, K. Laass, H. Holtmann, A. Kotlyarov, and M. Gaestel. 2012. The p38/MK2-driven exchange between tristetraprolin and HuR regulates AU-rich element-dependent translation. *PLoS Genet.* 8:e1002977. https://doi.org/10.1371/journal.pgen.1002977

Tokunaga, Y., K. Takeuchi, H. Takahashi, and I. Shimada. 2014. Allosteric enhancement of MAP kinase p38α's activity and substrate selectivity by docking interactions. *Nat. Struct. Mol. Biol.* 21:704–711. https://doi.org/10.1038/nsmb.2861

Uversky, V.N. 2017. Intrinsically disordered proteins in overcrowded milieu: Membrane-less organelles, phase separation, and intrinsic disorder. *Curr. Opin. Struct. Biol.* 44:18–30. https://doi.org/10.1016/j.sbi.2016.10.015

Waetzig, G.H., D. Seegert, P. Rosenstiel, S. Nikolaus, and S. Schreiber. 2002. p38 mitogen-activated protein kinase is activated and linked to TNF-alpha signaling in inflammatory bowel disease. *J. Immunol.* 168: 5342–5351. https://doi.org/10.4049/jimmunol.168.10.5342

Wang, W., N. Li, and X. Guo. 2023. The crosstalk between ILC3s and adaptive immunity in diseases. *FEBS J.* 291:3965–3977. https://doi.org/10.1111/febs.17014

Wang, W., Y. Li, J. Hao, Y. He, X. Dong, Y.-X. Fu, and X. Guo. 2020. The interaction between lymphoid tissue inducer-like cells and T cells in the mesenteric lymph node restrains intestinal humoral immunity. *Cell Rep.* 32:107936. https://doi.org/10.1016/j.celrep.2020.107936

Wegener, M., and M. Müller-McNicoll. 2018. Nuclear retention of mRNAs - quality control, gene regulation and human disease. *Semin. Cell Dev. Biol.* 79:131–142. https://doi.org/10.1016/j.semcdb.2017.11.001

Weis, F., E. Giudice, M. Churcher, L. Jin, C. Hilcenko, C.C. Wong, D. Traynor, R.R. Kay, and A.J. Warren. 2015. Mechanism of eIF6 release from the nascent 60S ribosomal subunit. *Nat. Struct. Mol. Biol.* 22:914–919. https://doi.org/10.1038/nsmb.3112

Xue, Y., J. Ren, X. Gao, C. Jin, L. Wen, and X. Yao. 2008. GPS 2.0, a tool to predict kinase-specific phosphorylation sites in hierarchy. *Mol. Cell. Proteomics*. 7:1598–1608. https://doi.org/10.1074/mcp.M700574-MCP200

Yang, W.L., W. Qiu, T. Zhang, K. Xu, Z.J. Gu, Y. Zhou, H.J. Xu, Z.Z. Yang, B. Shen, Y.L. Zhao, et al. 2023. Nsun2 coupling with RoRγt shapes the fate of Th17 cells and promotes colitis. *Nat. Commun.* 14:863. https://doi.org/10.1038/s41467-023-36595-w

Yang, X., Y. Yang, B.F. Sun, Y.S. Chen, J.W. Xu, W.Y. Lai, A. Li, X. Wang, D.P. Bhattarai, W. Xiao, et al. 2017. 5-methylcytosine promotes mRNA export - NSUN2 as the methyltransferase and ALYREF as an m^5C reader. *Cell Res.* 27:606–625. https://doi.org/10.1038/cr.2017.55

Zeng, B., S. Shi, G. Ashworth, C. Dong, J. Liu, and F. Xing. 2019. ILC3 function as a double-edged sword in inflammatory bowel diseases. *Cell Death Dis.* 10:315. https://doi.org/10.1038/s41419-019-1540-2

Zhang, C., G.R. Merana, T. Harris-Tryon, and T.C. Scharschmidt. 2022. Skin immunity: Dissecting the complex biology of our body's outer barrier. *Mucosal Immunol.* 15:551–561. https://doi.org/10.1038/s41385-022-00505-y

Zhao, X., Q. Di, H. Liu, J. Quan, J. Ling, Z. Zhao, Y. Xiao, H. Wu, Z. Wu, W. Song, et al. 2022. MEF2C promotes M1 macrophage polarization and Th1 responses. *Cell. Mol. Immunol.* 19:540–553. https://doi.org/10.1038/s41423-022-00841-w

Zheng, T., B. Zhang, C. Chen, J. Ma, D. Meng, J. Huang, R. Hu, X. Liu, K. Otsu, A.C. Liu, et al. 2018. Protein kinase p38α signaling in dendritic cells regulates colon inflammation and tumorigenesis. *Proc. Natl. Acad. Sci. USA*. 115:E12313–E12322. https://doi.org/10.1073/pnas.1814705115

Zhou, Y., B. Zhou, L. Pache, M. Chang, A.H. Khodabakhshi, O. Tanaseichuk, C. Benner, and S.K. Chanda. 2019. Metascape provides a biologist-oriented resource for the analysis of systems-level datasets. *Nat. Commun.* 10:1523. https://doi.org/10.1038/s41467-019-09234-6

Supplemental material

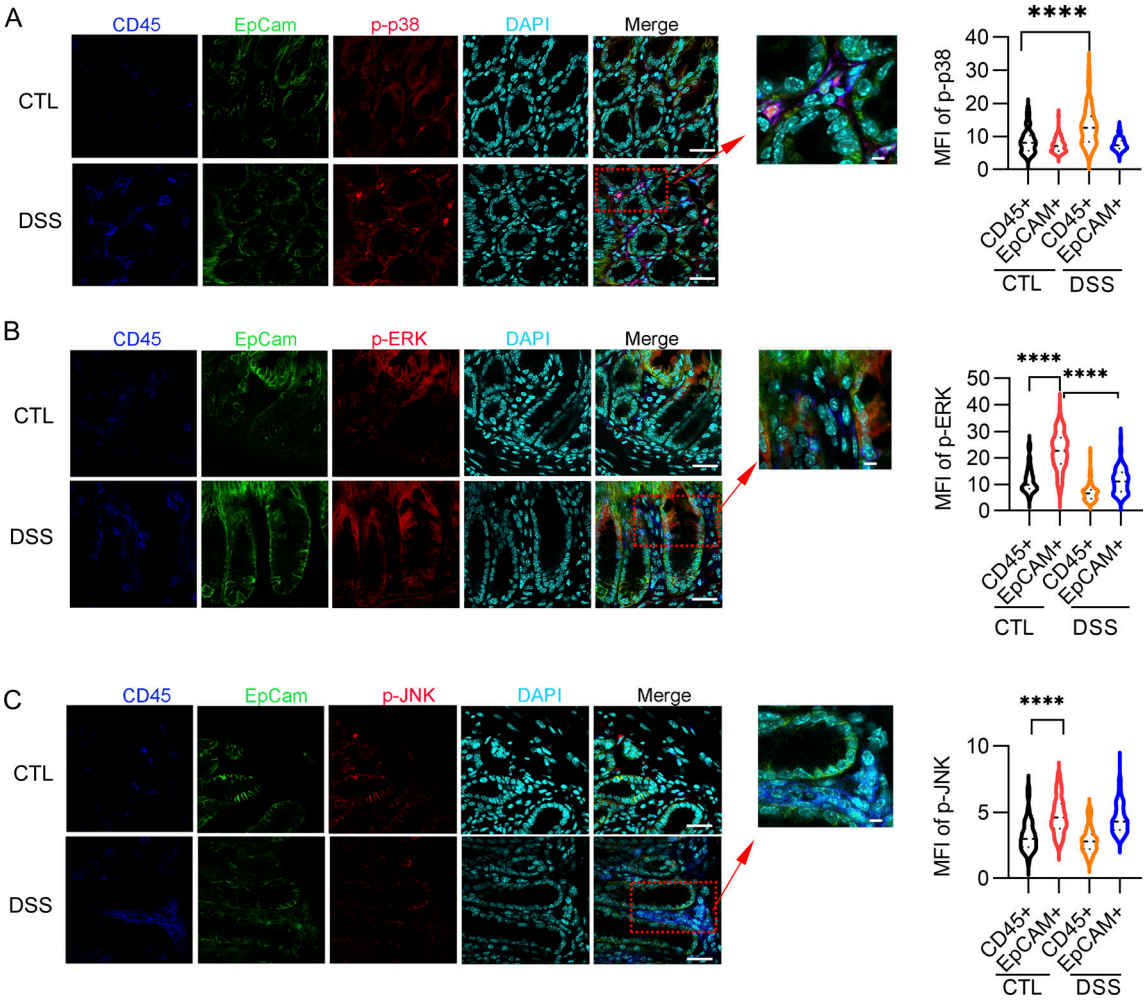

Figure S1. **The activation of MAPK signaling in the colon of DSS-induced colitis. (A–C)** 8-wk-old mice were exposed to the 3% DSS for 3 days and the colon was collected for cryosection. Representative colonic immunofluorescence images stained with antibodies against CD45 (blue), EpCAM (green), and different MAPKs including p-p38 (A, red), p-ERK1/2 (B, red) and p-JNK (C, red). Data are representative of one of two independent experiments. Scale bars, 20 µm; zoom-in scale bars, 4 µm. Data are mean ± SEM, and statistical significance was tested by two-tailed Student's unpaired *t* test (A–C), ****P < 0.0001.

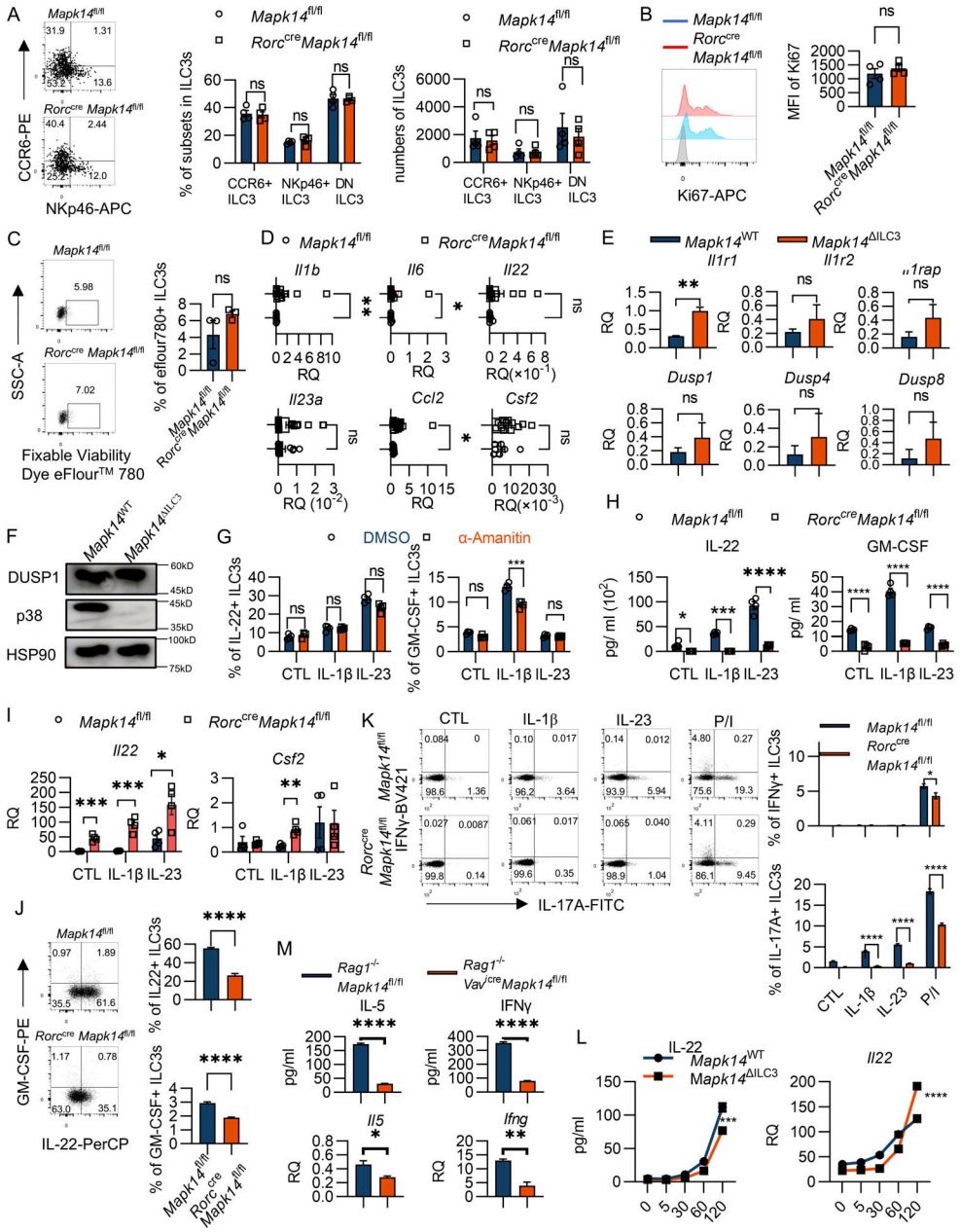

Figure S2. **p38α regulates ILC3 cytokine production. (A–C)** The colonic LPLs were isolated from naive *Rorc*^{cre}*Mapk14*$^{fl/fl}$ (n = 4) or *Mapk14*$^{fl/fl}$ (n = 4) littermate mice. Flow cytometry analysis of different subsets (A), cell proliferation by Ki67 (B), and cell viability by fixable cell viability dye (C) in ILC3s (gated in CD45$^+$CD90$^+$TCRβ$^-$RORγt$^+$) were shown. **(D)** 8-wk-old *Rorc*^{cre}*Mapk14*$^{fl/fl}$ and their littermates *Mapk14*$^{fl/fl}$ mice were given 3% DSS in drinking water for 6 days. The colon tissue was collected for RNA isolation and *Il1b*, *Il6*, *Ccl2*, *Il23a*, *Csf2*, and *Il22* expression in DSS-treated *Rorc*^{cre}*Mapk14*$^{fl/fl}$ (n = 12) and *Mapk14*$^{fl/fl}$ (n = 7) were measured by qPCR. Each symbol represents an individual mouse from two pooled experiments. **(E and F)** ILC3s were sorted from the small intestinal and colonic LPLs of *Rag1*$^{-/-}$*Mapk14*$^{fl/fl}$ and *Rag1*$^{-/-}$*Vav*^{icre}*Mapk14*$^{fl/fl}$ mice. **(E)** The mRNA expression of *Il1r1*, *Il1r2*, *Il1rap*, *Dusp1*, *Dusp4*, and *Dusp8* was measured by qPCR. **(F)** The protein expression of DUSP1 was examined by western blot. HSP90 was detected as a loading control. **(G)** LPLs from the intestinal lamina propria were pre-treated with or without α-amanitin and then stimulated with IL-1β and IL-23 in vitro. The production of IL-22 and GM-CSF by ILC3s (gated in eflour780$^-$CD45^{low}CD90^{high}) were detected by flow cytometry. **(H and I)** LPLs from *Rorc*^{cre}*Mapk14*$^{fl/fl}$ and *Mapk14*$^{fl/fl}$ mice were stimulated with IL-1β or IL-23 for 18 h. The protein (H) and mRNA expression levels (I) of IL-22 and GM-CSF were examined by ELISA and qPCR. **(J and K)** LPLs from the small intestinal and colonic lamina propria of *Rorc*^{cre}*Mapk14*$^{fl/fl}$ or *Mapk14*$^{fl/fl}$ littermate mice were stimulated with IL-23 or PMA/Ionomycin in vitro. The production of IL-22 and GM-CSF (J) or IL-17A and IFNγ (K) by ILC3s (gating in eflour780$^-$CD45^{low}CD90$^+$) was analyzed by flow cytometry. **(L)** ILC3s were sorted from the small intestinal and colonic LPLs of *Rag1*$^{-/-}$*Mapk14*$^{fl/fl}$ and *Rag1*$^{-/-}$*Vav*^{icre}*Mapk14*$^{fl/fl}$ mice and then were stimulated with IL-23 at different time points. The protein (left) and mRNA expression levels (right) of IL-22 were examined by ELISA and qPCR. **(M)** ILC2s (7-ADD$^-$CD45$^+$CD90$^+$CD3$^-$NK1.1$^-$KLRG1$^+$) and ILC1s (7-ADD$^-$CD45$^+$CD90$^+$ CD3$^-$NK1.1$^+$KLRG1$^-$) were sorted from small intestinal and colonic LPLs, and the expression of IL-5 in ILC2 (left) and IFNγ in ILC1 (right) at both protein (top) and mRNA (bottom) levels were evaluated by ELISA and qPCR. Data are representative of one of two independent experiments (A–C and E–M). Two experiments were pooled together (D). Each dot (A–D) represents one individual mouse. Each dot (G–I) represents one biological replicate. Data are mean ± SEM and statistical significance was tested by two-tailed Student's unpaired t test; *P < 0.05, **P < 0.01, ***P < 0.001, ****P < 0.0001; ns, no significant difference. Source data are available for this figure: SourceData FS2.

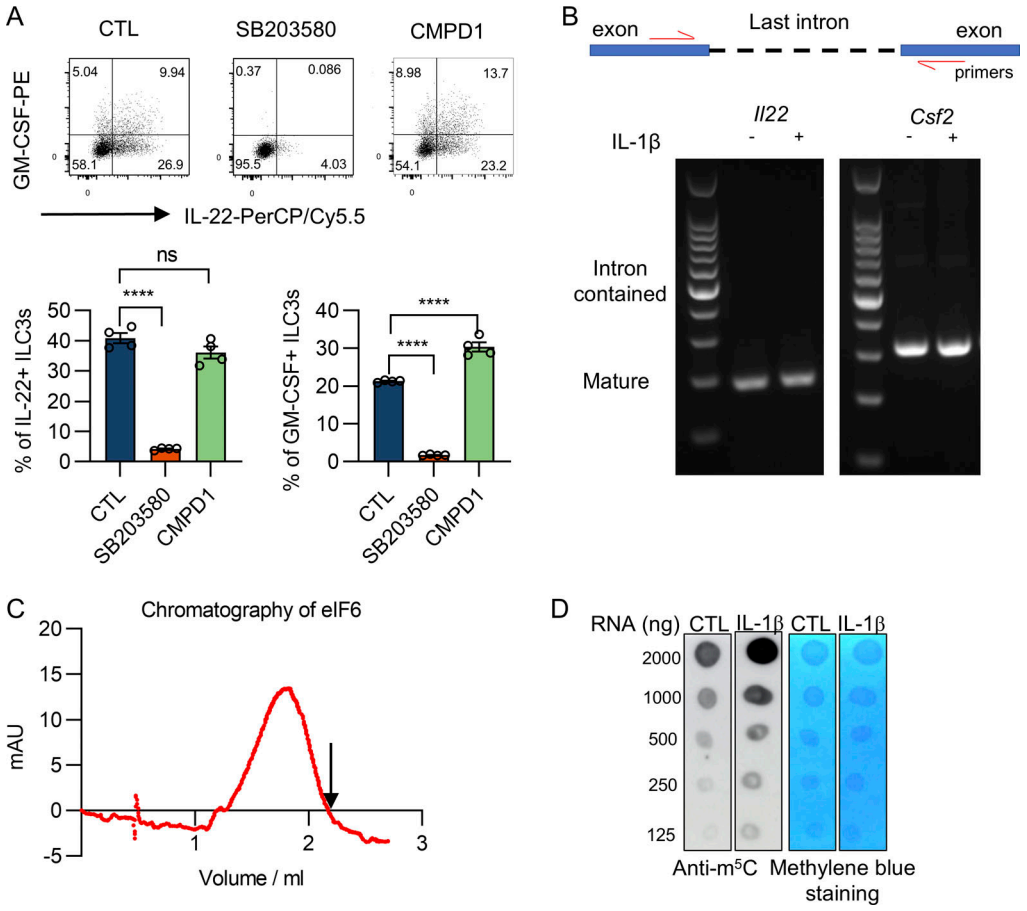

Figure S3. **p38α regulates the cytokine expression in ILC3s through eIF6. (A)** MK2 inhibition didn't affect ILC3 cytokine production. LPLs were pretreated with SB203580 and CMPD1 and then stimulated with IL-1β in vitro. IL-22 and GM-CSF production by ILC3s (gated in eflour780^{-}CD45^{low}CD90^{high}) were examined by flow cytometry. Data are representative of one of two independent experiments. Data are mean ± SEM and statistical significance was tested by two-tailed Student's unpaired *t* test; ****P < 0.0001; ns, no significant difference. **(B)** IL-1β treatment did not influence the IL-22 and GM-CSF mRNA splicing in ILC3s. The diagram for primer design to test maturation of *Il22* and *Csf2* mRNA. The mature or intron-contained premature mRNA was determined by RT-PCR and agarose gel electrophoresis. One of two independent experiments is shown. **(C)** The size exclusion chromatogram of purified eIF6. eIF6 displayed a significant advance in elution from the column compared with the predicted elution volume (indicated by arrow). One of two independent experiments is shown. **(D)** IL-1β promotes m^{5}C modification in MNK-3 cells. RNA dot blot analysis of mRNAs with m^{5}C modification in MNK-3 cells with or without IL-1β treatment. Total RNA was extracted from MNK-3 cells, crosslinked to the NC membrane, and detected by anti-m^{5}C antibody. The data are representative of at least two independent experiments. Source data are available for this figure: SourceData FS3.

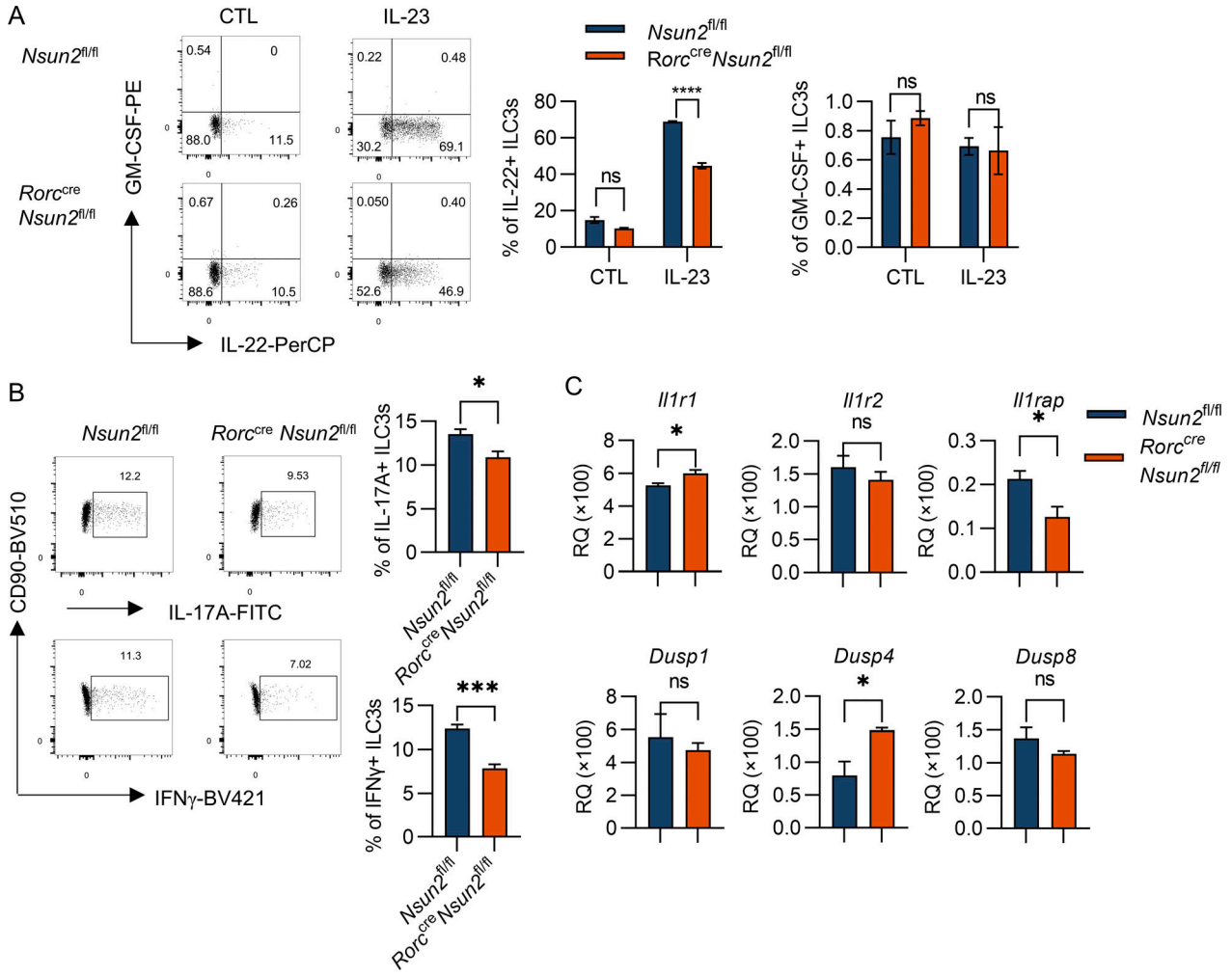

Figure S4. **Nsun2 regulates the expression of cytokines in ILC3s. (A)** LPLs from the small intestinal and colonic lamina propria of *Rorc*^{cre}*Nsun2*$^{fl/fl}$ or *Nsun2*$^{fl/fl}$ littermate mice were stimulated with IL-23 in vitro. The production of IL-22 and GM-CSF by ILC3s (gating in eflour780^{-}CD45^{low}CD90^{+}) was analyzed by flow cytometry. **(B)** LPLs from the small intestinal and colonic lamina propria of *Rorc*^{cre}*Nsun2*$^{fl/fl}$ or *Nsun2*$^{fl/fl}$ littermate mice were stimulated with PMA/Ionomycin in vitro. The production of IL-17A and IFNγ by ILC3s (gating in eflour780^{-}CD45^{low}CD90^{+}) was analyzed by flow cytometry. **(C)** ILC3s were sorted from the small intestinal and colonic LPLs of *Rorc*^{cre}*Nsun2*$^{fl/fl}$ or *Nsun2*$^{fl/fl}$ littermate mice. The mRNA expression of *Il1r1*, *Il1r2*, *Il1rap*, *Dusp1*, *Dusp4 and Dusp8* was measured by qPCR. Data are representative of one of two independent experiments (A–C). Data are mean ± SEM and two-tailed Student's unpaired *t* test; ns, no significance; *P < 0.05, ***P < 0.001, ****P < 0.0001.

A

Position	Code	Kinase	Peptide	Score	Cutoff
87	S	CMGC/GSK/GSK3B	ELQHIRNSLPDSVQI	6.878	6.68
239	S	CMGC/GSK/GSK3B	IATSMRDSLIDSLT*	9.568	6.68
243	S	CMGC/GSK/GSK3B	MRDSLIDSLT*****	7.263	6.68
87	S	CMGC/MAPK/p38/HOG1	ELQHIRNSLPDSVQI	4.265	3.652
239	S	CMGC/MAPK/p38/MAPK11	IATSMRDSLIDSLT*	40.997	37.247
243	S	CMGC/MAPK/p38/MAPK12	MRDSLIDSLT*****	125.57	118.354
91	S	CMGC/MAPK/p38/MAPK13	IRNSLPDSVQIRRVE	40.866	40.832
220	S	CMGC/MAPK/p38/MAPK13	TELSVVESVFKLNEA	41.393	40.832

B

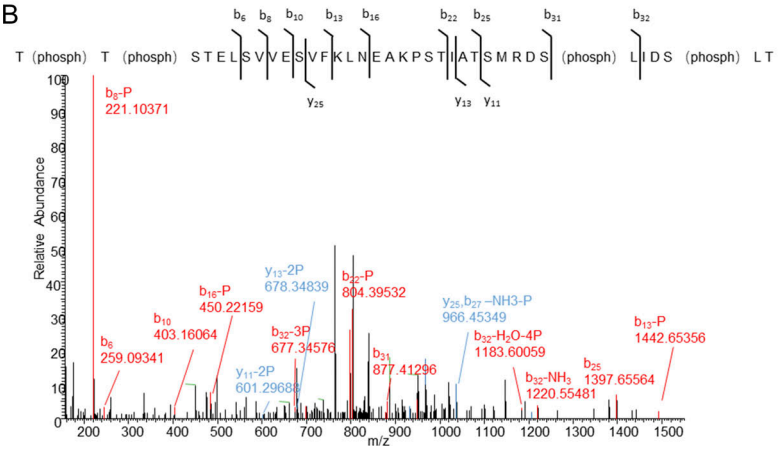

Figure S5. **The C-terminal of eIF6 was phosphorylated by p38α. (A)** The potential p38 and GSK3β phosphorylation sites of eIF6 predicted by group-based prediction system. **(B)** Multiple p38α phosphorylation sites on the C-terminal of eIF6 were identified by MS.

Provided online are Table S1, Table S2, Table S3, Table S4, Table S5, and Table S6. Table S1 shows the p38α-TurboID interactome. Table S2 displays the differential analysis of p38α interactome. Table S3 shows the *Il22* mRNA interactome. Table S4 displays the eIF6 interactome in ILC3s. Table S5 exhibits the components in both eIF6 and p38α interactome. Table S6 shows the sequence of qPCR primers.